



Directed energy deposition of Al 5xxx alloy using Laser Engineered Net Shaping (LENS®)

David Svetlizky ^a, Baolong Zheng ^b, Tali Buta ^a, Yizhang Zhou ^b, Oz Golan ^c, Uri Breiman ^d, Rami Haj-Ali ^d, Julie M. Schoenung ^b, Enrique J. Lavernia ^b, Noam Eliaz ^{a,*}

^a Department of Materials Science and Engineering, Tel-Aviv University, Ramat Aviv, Tel Aviv 6997801, Israel

^b Department of Materials Science and Engineering, University of California, Irvine, Irvine, CA 92697-2585, USA

^c School of Mechanical Engineering, Afeka – Tel Aviv Academic College of Engineering, Tel Aviv 6910717, Israel

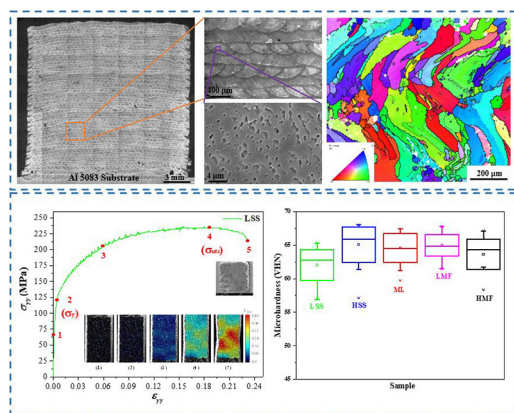
^d School of Mechanical Engineering, Tel-Aviv University, Ramat Aviv, Tel Aviv 6997801, Israel



HIGHLIGHTS

- Directed energy deposition of wrought-like Al 5xxx alloy by Laser Engineered Net Shaping is demonstrated for the first time.
- A transition in chemistry from an Al 5083 powder to one closer to Al 5754 in the as-deposited material is observed.
- A relative density as high as 99.26% is measured.
- The measured mechanical properties meet the requirements of international standards for wrought Al 5754-O.
- Various mechanisms may contribute to porosity formation in the deposited Al 5754, gas-related porosity being the major one.

GRAPHICAL ABSTRACT



ARTICLE INFO

Article history:

Received 6 February 2020

Received in revised form 27 April 2020

Accepted 28 April 2020

Available online 03 May 2020

Keywords:

Additive manufacturing (AM)

Aluminum alloys

Directed energy deposition (DED)

Laser Engineered Net Shaping (LENS®)

Mechanical properties

Micro-computed tomography (μ-CT)

ABSTRACT

Here, we present directed energy deposition (DED) of wrought-like Al 5xxx AlMg alloy by Laser Engineered Net Shaping (LENS®). A transition from an Al 5083 gas atomized powder feedstock to Al 5754 characteristics of the as-deposited material due to selective evaporation of Mg was observed. Density values obtained by X-ray micro-computed tomography (μ -CT) were compared to those obtained by the Archimedes method. The latter indicated a relative density as high as 99.26%. Possible origins of porosity are discussed. The as-deposited material was comprised of both equiaxed and columnar grains with no preferred crystallographic orientation and mean grain size of 36 μ m. The Young's modulus, yield stress, ultimate tensile strength, fracture strain, Poisson's ratio, and total ultimate strain energy (toughness) were determined by uniaxial tensile tests combined with digital image correlation (DIC). Fractography complemented the mechanical testing. A pulse-echo ultrasonic non-destructive test was used to obtain more accurate values of the Young's and shear moduli and to adjust the value of the yield strength accordingly. The measured mechanical properties meet the requirements of international standards for wrought Al 5754 in its annealed condition.

© 2020 The Authors. Published by Elsevier Ltd. This is an open access article under the CC BY-NC-ND license (<http://creativecommons.org/licenses/by-nc-nd/4.0/>).

* Corresponding author.

E-mail address: neliaz@tau.ac.il (N. Eliaz).

1. Introduction

Additive manufacturing (AM) provides energy and efficiency benefits when compared to traditional manufacturing processes [1,2]. The Laser Engineered Net Shaping (LENS®) process belongs to the branch of Directed Energy Deposition (DED) AM technologies. LENS® has been successfully used to process a variety of metallic, ceramic, metallic glass, composite, and functionally gradient materials (see Supplementary file), including aluminum-based materials [3–5].

Despite the success attained with various alloys, processing of high-quality structural Al alloys remains a challenge (as it is in other AM technologies such as Powder Bed Fusion, PBF, and in laser beam welding of aluminum alloys). This challenge is related mainly to the inherent properties of Al and its raw powder feedstock: (1) Al is characterized by high surface reflectivity [6–9] and high thermal conductivity [10,11]. Consequently, high cooling rates might lead to cracking, whereas excessive thermal energy accumulation during processing might lead to formation of pores, cracks and other defects [7]. Hence, high laser power is required to allow proper melting and deposition of Al powders [12]. (2) Increased laser energy may promote selective evaporation of alloying elements with low boiling point such as Zn and Mg. This could result in gas porosity in the deposited Al alloy and degradation of mechanical properties. In addition, fluctuation in alloy composition and hot cracking occur easily during laser cycling [7]. (3) Due to their wide range of solidification temperatures and high thermal expansion coefficient ($\alpha = 27.5 \times 10^{-6} \text{ 1/K}$), rapid solidification might be associated with high levels of residual stresses, resulting in cracking and deformation of the as-deposited material [7]. (4) Poor powder flowability due to the low density of the Al alloy powder along with low viscosity of molten Al alloys [13]. This may cause unstable powder flow into the melt pool and result in unstable deposition and subsequent porosity [14–16]. (5) Moisture absorption in Al alloy powders is high. Since the solubility of hydrogen in molten Al is more than 19 times higher than in solid Al, hydrogen-related porosity may form when the melt solidifies rapidly [7]. (6) Al is highly susceptible to oxidation. The native oxide on the raw powder feedstock has high melting temperature (2066 °C), may reduce the melt-pool wettability, cause oxide inclusions in the as-deposited material [17], and promote porosity [18,19]. Therefore, strict requirements exist for oxygen partial pressure (or vacuum) of the processing environment.

All of the above listed challenges play a significant role in hindering the development of adequate Al-based alloys using either PBF or DED technology. To date, only a few Al alloys have been printed with sufficiently high quality, the most common ones being AlSi [3,20–24] and AlSiMg [14,25–27] alloys due to their good tensile and fatigue properties, good weldability, and corrosion resistance [28]. The main reason for the popularity and the extensive study of these alloys is the high Si content, which increases the wettability properties of the melt pool and decreases the shrinkage [16,29]. In related work, Ramesh [4] utilized both LENS® and selective laser melting (SLM) processes and studied the microstructure development and hardness of AlSi10Mg alloy. Refinement of the microstructure was observed along the build direction in both cases. This result is consistent with published studies [25,26], which also showed anisotropy of the mechanical properties and a reduction in hardness along the deposition direction. These phenomena were attributed to Si particle size variations and distribution along the build as well as variations in microstructural morphology.

To date, very limited work has been reported on AM of non-heat-treatable Al alloys in general, and AlMg alloys specifically. Olakanmi [17] investigated AM of AlMg6 alloy at various processing parameters using SLM. Results show that the deposition of AlMg6 is highly dependent on the deposition energy density – low energy densities resulted in a network of agglomerates with many pores of different types. At the highest energy density applied (30 J/mm²), the best deposit had average material density of 1.4 g/cm³ and average hardness of 265 VHN. However, tensile properties and post-deposition chemical analysis

were not reported. Mauduit et al. [30] investigated the suitability of various Al alloys for AM using the SLM technique and various process parameters. Among others, deposition of Al 5083 was reported. A reduction of approximately 29% in the Mg concentration after laser deposition due to selective evaporation of Mg, substantial intergranular hot cracking, and porosity were reported. Nevertheless, mechanical properties and material density values were not reported. Recently, Zhou et al. [31] studied the effects laser scan speed and laser power on the microstructure and mechanical properties of Al 5083 alloyed with 0.7 wt% zirconium (Zr) and deposited by SLM. A refined microstructure and improved properties resulted from Zr alloying. Furthermore, a qualitative processing parameter correlation was proposed, showing the effect of laser scan speed and laser powder on the obtained density.

In this study, DED of Al 5083 powder was studied. In its wrought form, this alloy has excellent corrosion resistance, good weldability and formability, and excellent strength compared to other non-heat-treatable alloys [32]. Yet, very little has been reported on laser-based AM of Al 5083. Here, we present for the first time [33] an extensive investigation of Al 5xxx alloy deposition using the LENS® process. This includes chemical composition, microstructure, porosity, density, and mechanical behavior.

2. Materials and methods

2.1. Powder feedstock

A pre-alloyed Al 5083 powder was processed by TLS Technik GmbH & Co. (Bitterfeld-Wolfen, Germany), using a gas atomization (GA) process. Powder feedstock characterization was performed to confirm the quality of the custom-made powders in terms of morphology, chemical composition, powder sphericity, and size distribution (Figs. S1 & S2, Supplementary file). The chemical composition of the powder feedstock was analyzed by inductively coupled plasma optical emission spectrometry (ICP-OES, PlasmaQuant PQ9000, Analytik Jena AG, Jena, Germany). The oxygen content in the feedstock powder was measured by an ONH-2000 oxygen/nitrogen/hydrogen analyzer (Eltra GmbH, Haan, Germany) that is based on the inert gas fusion technique. XRD measurements of the powder feedstock were performed using a D8 ADVANCE diffractometer (Bruker AXS, Madison, WI, USA) and Cu-K α radiation source. Phase identification, reflection indexing and estimation of the phase contents were made with the aid of TOPAS software, ver. 5 (Bruker AXS, Madison, WI, USA).

2.2. LENS® deposition process

LENS® deposition process was carried out using a 750 LENS® machine (Optomec, Inc., Albuquerque, NM, USA). This system combines a controlled environment glove box and a high power (up to 1000 W) continuous wave Nd:YAG laser (IPG Photonics, Inc., Oxford, MA, USA) at a wavelength of 1064 nm [34]. Five block samples, with the dimensions of 60 × 15 × 15 mm, were processed on an Al 5083 plate substrate (which was initially in the H131 temper condition, but may have been locally annealed during the DED thermal cycles). All samples were deposited according to the following sequence: the first three layers were deposited at laser power of 800 W, followed by 12 layers at laser power of 650 W, followed by decreasing the laser power to 600 W until the end of the designed geometry. The related zones in the deposited alloy will be termed hereafter Zone 1, Zone 2, and Zone 3, respectively (see Fig. 1A). The gradual decrease in the laser power was aimed to overcome high back-reflection protection of the laser system and to allow surface temperature buildup that enables proper deposition. It should be noted that this study was mainly focused on the characterization of Zone 3, because Zones 1 and 2 are usually removed during disconnection of the deposited part from the substrate. The thickness between successive layers was set at 0.254 mm, with a hatch spacing of 0.406 mm between adjacent deposits and a laser

beam diameter of 0.5 mm. The laser energy density per unit area was calculated using Eq. (1) [35]:

$$I = \frac{P}{\nu D} \quad (1)$$

where P is the laser power, ν is the laser scan speed, and D is the laser beam diameter projected on the substrate. Deposition was performed under argon environment, keeping the oxygen level below 20 ppm to avoid oxidation during deposition. The initial oxygen level was 19.6 ppm; it decreased over time to 16.1 ppm. The rest of the processing parameters used in this study and relevant for Zone 3 are given in Table 1. Hereafter, LMF is the low powder mass flow rate level, HMF is the high powder mass flow rate level, LSS is the low scan speed level, HSS is the high scan speed level, and ML is the middle level for both factors. The deposition strategy used an angle of 90° between the hatch lines of two adjacent layers.

2.3. Sample preparation for microstructural and mechanical characterization

The three-dimensional deposited samples ($15 \times 15 \times 60$ mm, see Fig. 1A) were sectioned into cross-sections (orange zone in Fig. 1A) and ground using 320 grit SiC paper, followed by polishing with diamond suspensions (9, 3, and 1 μm). Final polishing was done using 0.2 μm and 0.05 μm colloidal silica suspensions. For the microstructural investigation, the polished samples were chemically etched using Keller's reagent (2 mL HF, 3 mL HCl, 5 mL HNO₃, 190 mL DI water).

Table 1

LENS® powder mass flow rate, laser scan speed and laser energy density processing parameters for Al 5xxx. Laser power was 600 W in all cases.

Sample	Scan speed (mm/s)	Mass flow rate (g/min)	Energy density (J/mm ²)
LMF	21	15	56
ML	21	25	56
HMF	21	33	56
LSS	17	25	70
ML	21	25	56
HSS	25	25	47

For mechanical properties investigation, tensile samples were fabricated (green zone in Fig. 1A) using a wire electrical discharge machining (EDM) system (FA20S, Mitsubishi Electric Corp., Tokyo, Japan). The dimensions of the tensile test samples are presented in Fig. 1B. Prior to tensile testing, the specimens were ground on 600 grit followed by 800 grit SiC papers, in order to remove surface porosity and other defects introduced by EDM and detected by light microscope inspection. The tensile sample geometry was validated by performing prior tensile tests of reference samples made of wrought Al 5083-O combined with digital image correlation (DIC) analysis. Tensile sample preparation included spraying black and white paint colors on the surface of the Al samples in order to achieve a randomly distributed speckles pattern with sufficient contrast for the DIC post-processing algorithm. All analyzed reference samples fractured within the gage and yielded mechanical property values in accordance with the requirements of ISO-BS-EN 485-2:2016 standard [36].

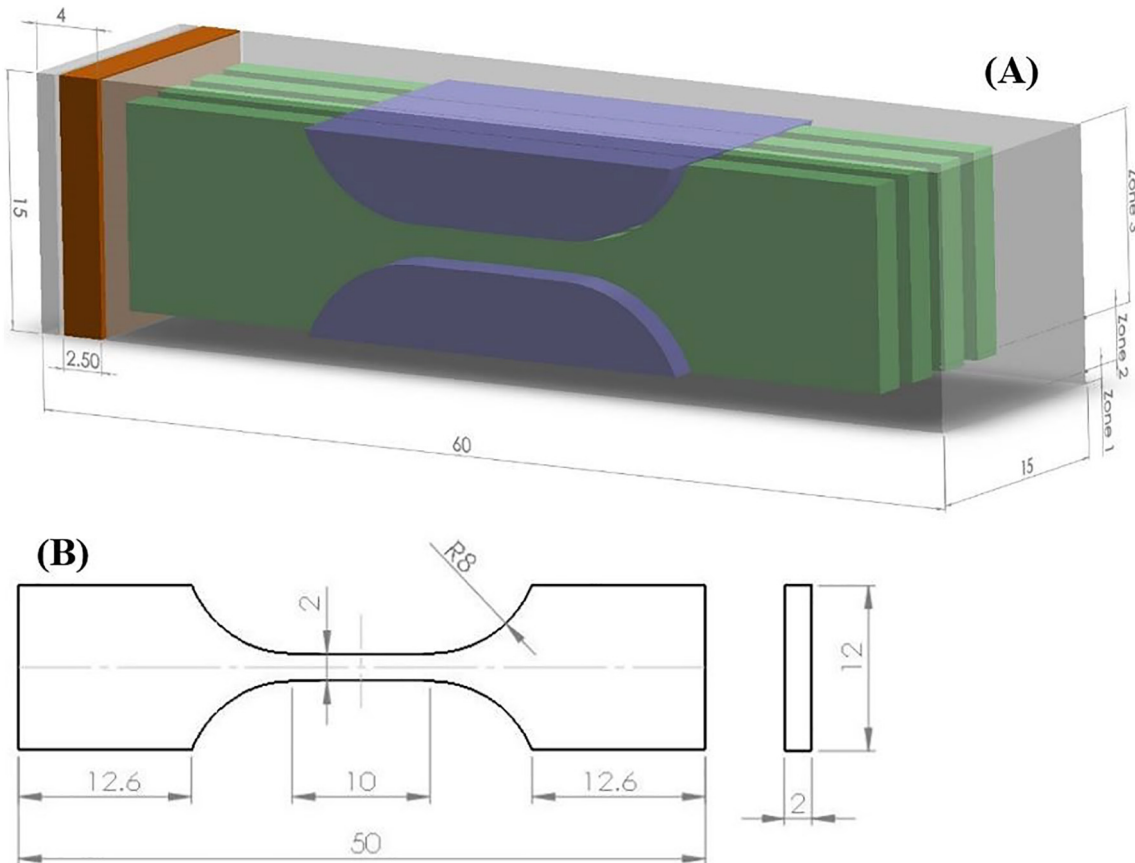


Fig. 1. (A) Schematic diagram showing from where samples for different characterization techniques were extracted from the Al 5xxx DED builds, and their dimensions (in mm). Colors scheme: grey – as-deposited sample; blue – chemical analysis and Archimedes density measurements; green – Archimedes density measurements, μ -CT, tensile tests, and pulse-echo ultrasonic tests; orange – EBSD, SEM, EDS, and XRD. The three deposition zones deposited at different laser power values are marked Zone 1 (800 W), Zone 2 (650 W), and Zone 3 (600 W). (B) Tensile test dimensions (mm).

2.4. Physical, chemical and microstructural characterization

The bulk relative density of the deposited samples was measured according to the Archimedes principle using a BA 210 S balance with 0.1 mg readability and density determination kit (Sartorius AG, Göttingen, Germany). The samples were weighed in deionized (DI) water at room temperature. A surfactant was added to reduce their surface energy and allow full infiltration of water into any open pores or asperities at the surface of the sample. The calculated values were expressed as relative density (percentage), assuming that the density of fully dense Al 5083 is 2.66 g/cm³. μ-CT scans were made using an EasyTom system (RX Solutions, Chavanod, France) equipped with a 150 kV generator and six linear motorized axes for optimized magnification. The current was 200 μA, the spot size 5 μm, and the resolution (voxel size) 36 × 36 × 36 μm. Each scan consisted of 1440 slices employing a 360° rotating stage. X-Act software was used for reconstruction while quantitative analysis was performed using VGStudio MAX 3.0 software (Volume Graphics GmbH, Heidelberg, Germany) with porosity analysis module. Pore diameter and pore sphericity were analyzed using a threshold algorithm implemented in the software. The microstructure of polished cross-sections was characterized by a light microscope (AX10, ZEISS, Oberkochen, Germany), SEM (Quanta 200 FEG, FEI, USA) equipped with an energy dispersive X-ray spectroscopy (EDS) silicon drift detector (X-Max SDD, Oxford Instruments, High Wycombe, UK) with 127 eV resolution and element analysis down to Boron, and EBSD detector (NORDLYS II, Oxford Instruments, High Wycombe, UK) with Aztec processing software. XRD (D8 ADVANCE diffractometer, Bruker AXS, Madison, WI, USA) complemented the microstructure analysis. Chemical analysis of the *as-deposited* material was conducted by a metal analysis OES spectrometer (Vario Lab, Belec Spektrometrie Opto-Elektronik GmbH, Georgsmarienhütte, Germany). The oxygen content in the *as-deposited* alloy was measured by an ONH-2000 oxygen/nitrogen/hydrogen analyzer (Eltra GmbH, Haan, Germany).

2.5. Mechanical properties characterization

To investigate the mechanical properties of the LENS® deposited Al 5xxx samples, Vickers microhardness testing was performed under 50 g load for 15 s, according to ASTM E384 – 17. Uniaxial tensile tests combined with DIC [37,38] were also performed to determine the Young's modulus, yield stress, ultimate tensile strength, fracture strain, Poisson's ratio, and total ultimate strain energy (toughness). The tensile tests were performed using an Instron 5582 machine equipped with a 50 kN load cell under a constant cross-head displacement rate of 0.1 mm/min. DIC data and post-processing were performed using DaVis 10

software package (LaVision GmbH, Göttingen, Germany). The sum of differential algorithm was used as a correlation technique for displacement tracking and strain calculation. In this method, the deformation of each image is defined as the sum of the differentials of the preceding images. Two LaVision 5 MP, 12-bit CCD digital cameras were used: one equipped with a 105 mm Nikon HS-14 lens to view the full gage area, the other equipped with a × 12 magnification Navitar lens to view the middle-gage area in order to capture the axial and transverse strains, respectively. A recording frame rate of 2 Hz was used and synchronized with the Instron load data. The dual camera setup is necessary, in part, for determination of the Poisson's ratio.

The elastic constants were also measured using the dynamic pulse-echo ultrasonic non-destructive test (NDT) with a time-of-flight (TOF) sound velocity analysis [39]. The "dynamically" measured Young's modulus and Poisson's ratio were compared to those obtained from tensile test in conjunction with DIC. The ultrasonic longitudinal and transverse wave propagation velocities through the specimen thickness (v_L and v_T , respectively) were thus measured. The ultrasonic wave propagation velocity was first measured for a Krautkrämer's reference block made of steel (with a thickness $d = 2.556$ mm), thus estimating the accuracy to be 1.3%. A standard 10 MHz probe was then used for v_L measurements on deposited specimens ($d = 1.79\text{--}2.31$ mm). For the v_T measurements, we used a 4 MHz normal incidence shear-wave transducer with high viscosity couplant. The advantages and disadvantages of dynamic methods compared to static methods are listed in the Supplementary file along with the equations used for the deduction of the elastic constants.

3. Results

3.1. Chemical composition of the powder feedstock vs. the *as-deposited* alloy

To study the effect of the LENS® process parameters on the chemical composition, both the Al 5083 powder feedstock and the *as-deposited* Al alloy samples were characterized. The results are shown in Table 2. The chemical composition of the powder feedstock meets the standard requirements for Al 5083 [40,41]. However, as a result of reduction in the concentration of Mg (and Zn) in the *as-deposited* alloy, its chemical composition more closely matches the requirements for wrought Al 5754 [40,41]. The oxygen content was 610 and 608 ppm (wt.) in the powder feedstock and *as-deposited* alloy, respectively.

In order to examine the possibility that pores originated from the selective evaporation of Mg, EDS line-scan analysis was performed across random spherical pores in metallographic cross-sections. No

Table 2
Chemical composition (wt%) of gas-atomized Al 5083 powder feedstock and *as-deposited* Al 5xxx alloy. For comparison, the standard requirements for wrought Al 5083 and Al 5754 alloys [40,41] are also provided.

Material	Mg	Mn	Cr	Si	Fe	Zn	Ti	Cu	Al
GA powder ^d	4.527 ^e	0.544	0.005	0	0.242	0.027	0.006	0.004	Bal.
LSS ^{f,g}	2.743	0.477	0.051	0.262	0.230	0	0	0.002	Bal.
HSS ^{f,g}	2.879	0.482	0.055	0.335	0.204	0	0	0.004	Bal.
ML ^{f,g}	2.649	0.465	0.046	0.260	0.218	0	0	0	Bal.
LMF ^{f,g}	2.861	0.459	0.043	0.249	0.207	0	0	0	Bal.
HMF ^{f,g}	2.628	0.462	0.050	0.293	0.215	0	0	0	Bal.
Al 5083 ^c	4.0–4.9	0.40–1.0	0.05–0.25	0.40 ^a	0.40 ^a	0.25 ^a	0.15 ^a	0.10 ^a	Bal.
Al 5754 ^c	2.6–3.6	0.50 ^b	0.30 ^b	0.40 ^a	0.40 ^a	0.20 ^a	0.15 ^a	0.10 ^a	Bal.

^a Maximum value.

^b 0.10–0.60 Mn + Cr.

^c Each other element: maximum 0.05 wt%. Total other elements: maximum 0.15 wt%.

^d ICP-OES.

^e OES.

^f See Table 1.

^g Mean values. The total concentration of other elements in these alloys was 0.113–0.116 wt%.

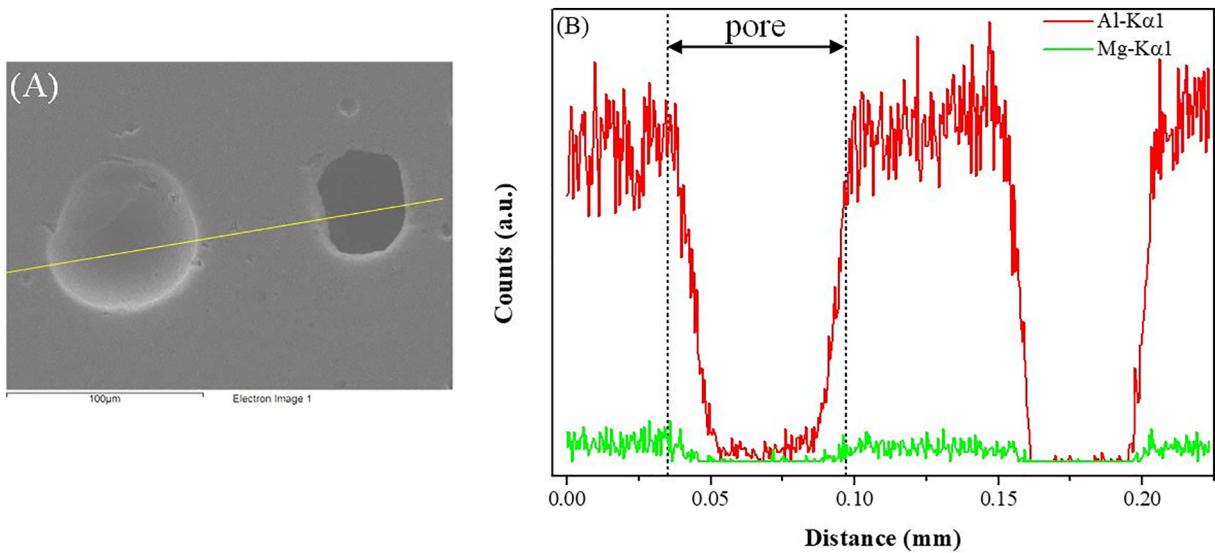


Fig. 2. (A) SEM image of pores in the cross-section of the as-deposited 5xxx bulk samples. (B) Representative EDS line-scan across the left, spherical pore in (A).

noticeable accumulation of Mg at the pore surface was discovered (Fig. 2).

3.2. The effect of deposition conditions on material density and porosity

In this work, we employed both the Archimedes method and μ -CT tests in order to measure the density of the deposited material. The mean relative densities of the as-deposited samples measured using the Archimedes method varied between 96.06% and 99.26%, depending strongly on the processing variables, such as powder mass flow rate (which is controlled by the argon flow rate) and laser scan speed (Fig. 3). Although the processing parameters still require additional optimization to achieve near full density, the observed process window shows that both the powder mass flow rate and the laser scan speed directly affect the deposited Al alloy density. The attained highest density was observed in sample ML, which is defined as the middle level in both investigations performed. On the other hand, the least dense samples were HSS (96.06%) and LMF (96.09%), which were processed with the highest laser scan speed and lowest energy density (HSS), or lowest powder mass flow rate (LMF). Furthermore, increased density was also observed in samples that were fabricated at high powder mass flow rate (or, high argon flow rate).

Porosity and density analysis was also made using μ -CT. A representative μ -CT illustration of pore diameter and pore sphericity in sample LSS is shown in Fig. 4. The pore size and pore sphericity population histograms with the corresponding cumulative distributions for different samples are presented in Figs. 5 & 6, respectively. Spherical pores were observed scattered throughout the deposited samples. Surprisingly, the μ -CT sphericity analysis indicated that the sphericity factor of the analyzed pores does not exceed 0.81 in any of the analyzed samples. Still, ~80% of the pores in all samples are characterized by a sphericity factor of 0.6 and higher. A summary of the relative densities analyzed utilizing both the Archimedes and μ -CT techniques is presented in Fig. 7. Values obtained from μ -CT are found to be lower.

3.3. Microstructure characterization

A light microscope composition image of a chemically etched cross-section of an as-deposited sample is shown in Fig. 8A. Zones 1, 2 and 3, defined in Section “LENS® deposition process” and in Fig. 1A are marked in this figure. Some porosity is evident, in particular in the first deposited layers adjacent to the base plate. A mesh-like morphology is noticeable throughout the entire deposit; it consists of horizontal and vertical

curved thin interfaces that are light contrasted in the optical micrograph and dark contrasted in the SEM images (Fig. 8B,C). The vertical and horizontal interfaces correspond to the molten metal flow trails and inter-

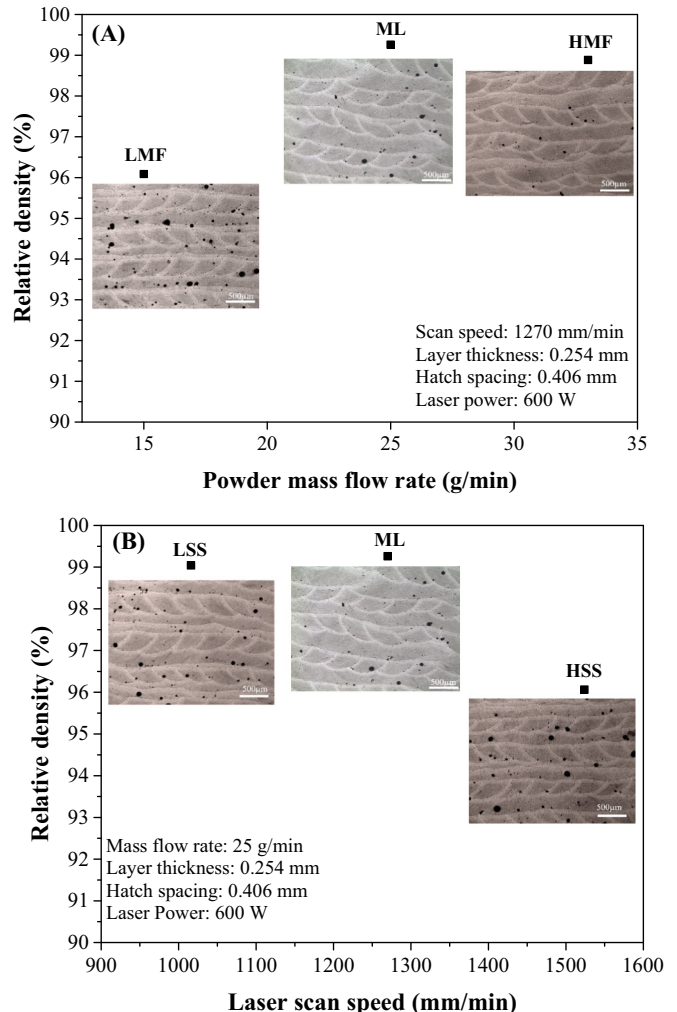


Fig. 3. The effect of deposition conditions on the relative density of the as-deposited Al alloy bulk samples, as a function of: (A) powder mass flow rate. (B) Laser scan speed.

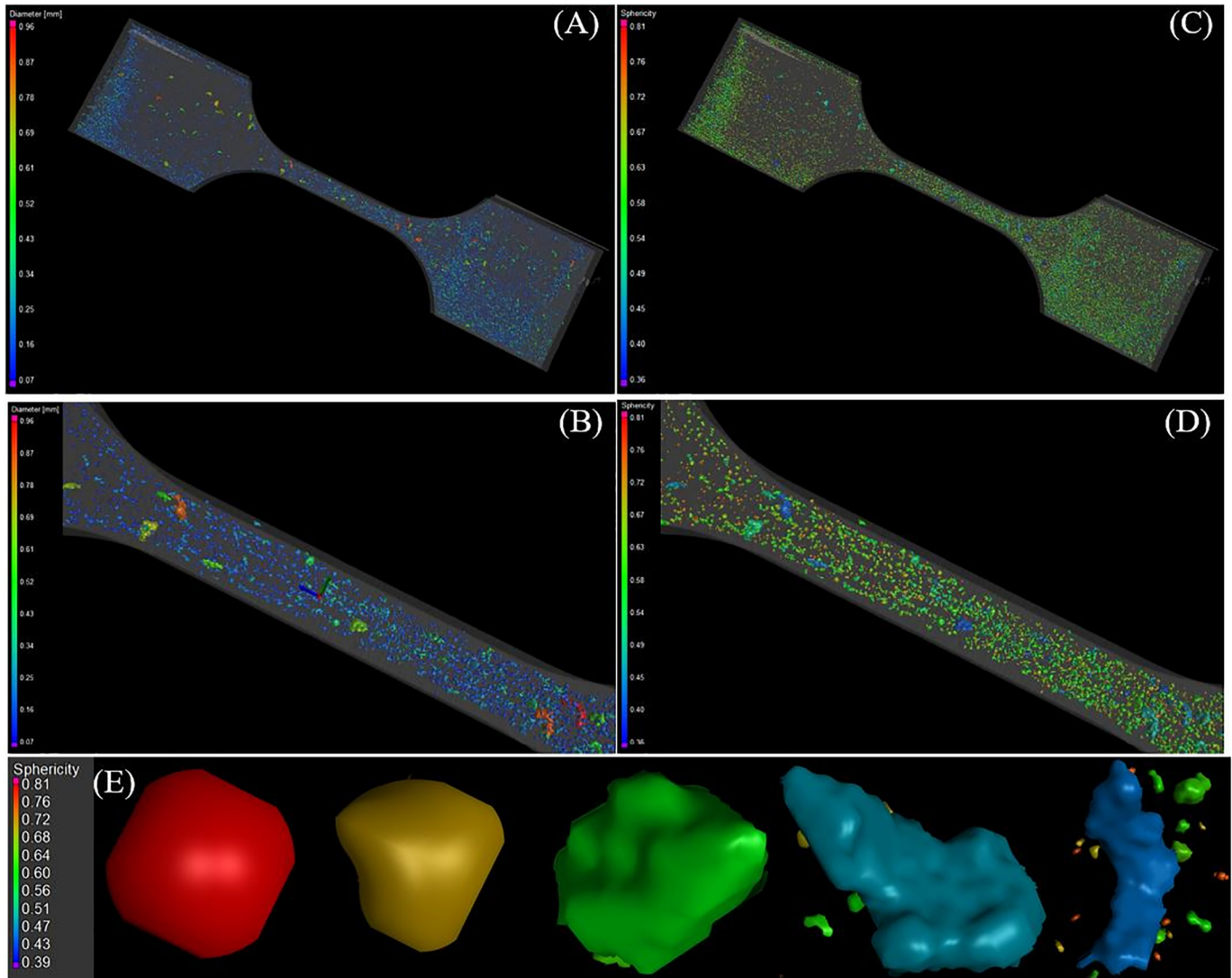


Fig. 4. μ -CT spatial reconstruction images of a representative tensile test sample of LSS sample (tensile test sample dimensions are presented in Fig. 1). (A) Pore diameter illustration. (B) Magnification of the gage area in (A). (C) Pore sphericity illustration. (D) Magnification of the gage area in (C). (E) Selected representative types of sphericity morphology.

pass boundaries, respectively. Fig. 8B,C also reveals a continuous layer between every two adjacent layers with mesh-like morphology. This structure reflects the deposition strategy of 90° rotation between the hatch lines of two adjacent layers. Consequently, in the microscope images we observe alternating longitudinal and transverse cross-sections of deposition tracks. Importantly, the metal flow trails and inter-pass boundaries appear to be well fused throughout the deposited sample. This can be related to epitaxial interfaces [34]. In addition, no evidence of hot cracking is observed in the sample. The inter-pass heat affected zone (HAZ) originated from repetitive thermal exposure during laser-based deposition [34] is shown in Fig. 8D.

Fig. 8E,F reveals some differences in the microstructure in two distinct zones in a single solidification cell. In both zones, however, pores left behind a selectively etched (more chemically active) phase are evident. The exact identification of the selectively etched phase, which is surrounded by an α -Al matrix, has yet to be determined. However, given the chemical composition of this alloy, it can be speculated that this phase is rich in Mg. Its areal fraction in Fig. 8E,F is high enough to expect it to be detectable by XRD, for example. As will be shown below, this is indeed the case. Fig. 8G shows a magnification of the area marked in red rectangle in Fig. 8A. A defect is noticeable, which illustrates porosity with irregular morphology related to lack of fusion

where inclusions of un-melted particles are entrapped in between the unbounded surfaces.

EBSD analysis was done to characterize the microstructure of the as-deposited alloy in terms of crystallographic orientation, grain size, and the grain morphology. Fig. 9B presents an orientation map of the analyzed cross-section shown in Fig. 9A using inverse pole figure coloring. This map is comprised of both equiaxed and columnar grains. Furthermore, epitaxial growth of the grains is evident, as the deposited layer grows with the same crystallographic orientation as its former. This results in columnar grains. In addition, a tilt growth angle can be observed. The pole figures in Fig. 9C show that in all principal orientations {111}, {101} and {001}, only weak texture exists. This indicates a random grain orientation with no preferred crystallographic orientation. The grain size and aspect ratio distributions of the analyzed cross-section are presented in Fig. 9D,E.

XRD analysis was done to identify the phases in the as-deposited Al alloy (ML sample) and compare them to those in the as-received GA powder feedstock and in wrought Al 5083-O (Fig. 10). The Al 5083 sample was sectioned from the base plate on which deposition was done, and standard annealing heat treatment was conducted prior to XRD analysis. TOPAS Rietveld refinement indicated (weighted profile R -factor, $R_{wp} \approx 10.3$) that the as-deposited alloy is comprised of 94.55 wt

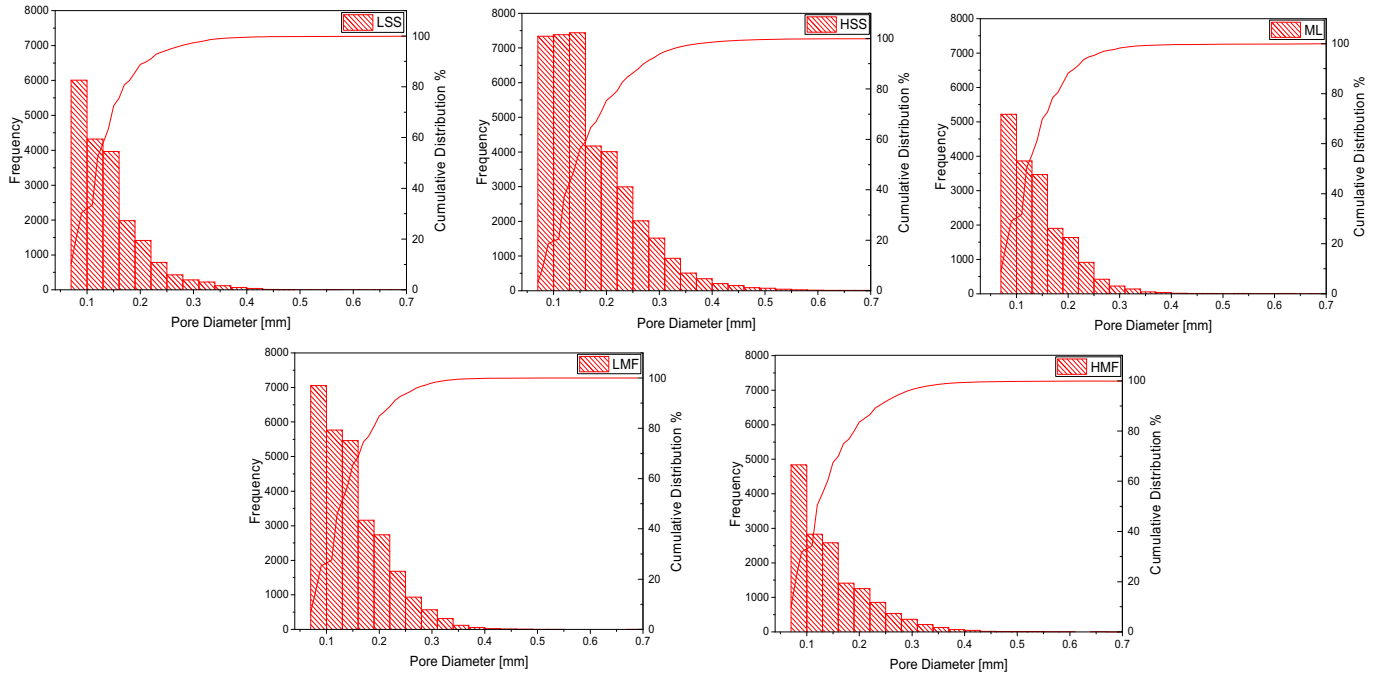


Fig. 5. Pore diameter population histograms and cumulative distributions based on μ -CT analysis.

% pure fcc Al (card #04-012-7848, lattice parameter $a = 4.0509 \text{ \AA}$), 2.62 wt% solid solution of Mg in Al (card # 04-003-7061, Al0.9547 Mg0.0453, fcc, $a = 4.0646 \text{ \AA}$), and 2.83 wt% pure Mg (card #00-035-0821, hcp, $a = 3.20936 \text{ \AA}$, $c = 5.2112 \text{ \AA}$). The only two reflections of the Mg phase evident in Fig. 10 are the two strongest reflections of this phase according to the card, namely (101) at $2\theta = 36.619^\circ$ and (002) at $2\theta = 34.398^\circ$, which makes the identification of the phase based on only two reflections legitimate. The XRD-TOPAS analysis is consistent with the SEM characterization presented above, according to which the as-deposited alloy is comprised of a minor amount of Mg-rich phase surrounded by an Al matrix. The XRD results are also in good agreement with the EBSD analysis with respect to the crystallographic orientation. Finally, one could compare the chemical

composition of the ML sample calculated based on the TOPAS analysis above to that measured by OES and reported in Table 2. The former is obtained by multiplying the concentration of phase i that contains element j by the concentration of the element in that phase, and then summing-up all relevant phases. Thus, we estimate that the concentrations of Al and Mg in the as-deposited sample ML are 97.051 wt% and 2.949 wt%, respectively. The corresponding values obtained from OES are 96.362 wt% and 2.649 wt%, respectively. Thus, there is good agreement, in particular when recalling that the TOPAS analysis did not take into account any other element except Al and Mg. Returning to Fig. 10, no significant difference is noticeable between the diffraction patterns of the GA powder, the as-deposited alloy, and wrought Al 5083-O, except some intensification of the (111) reflection in the as-

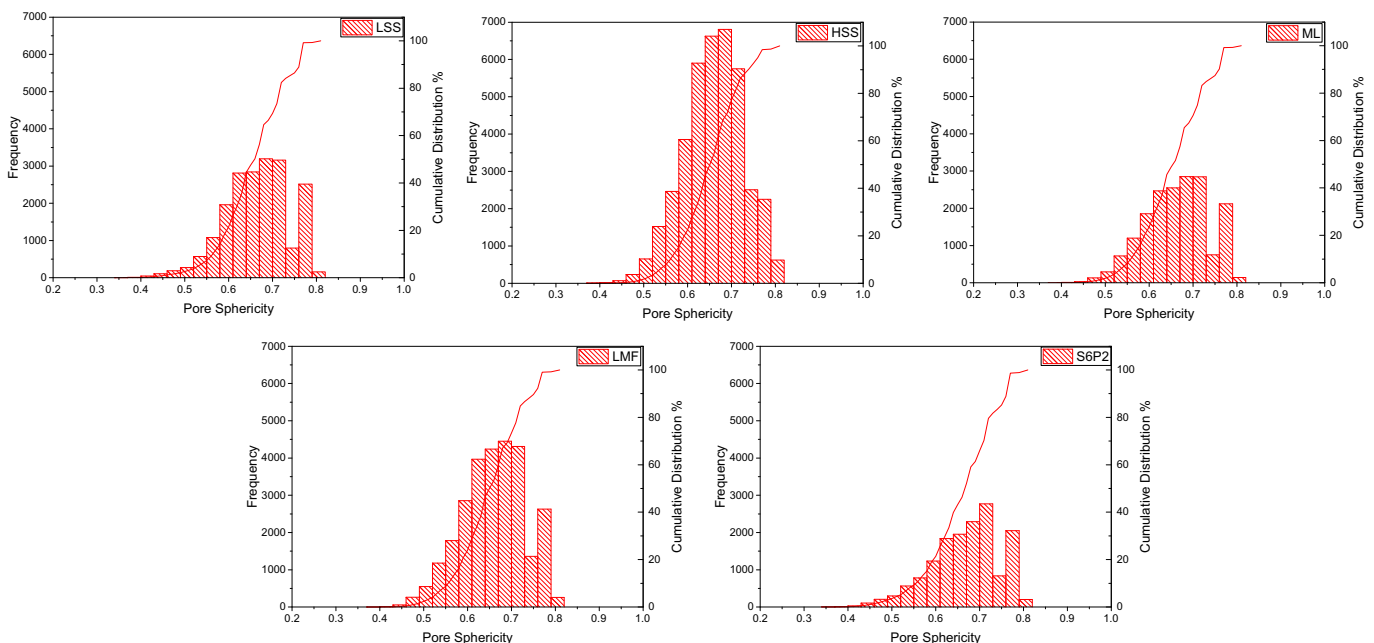


Fig. 6. Pore sphericity population histograms and cumulative distributions based on μ -CT analysis.

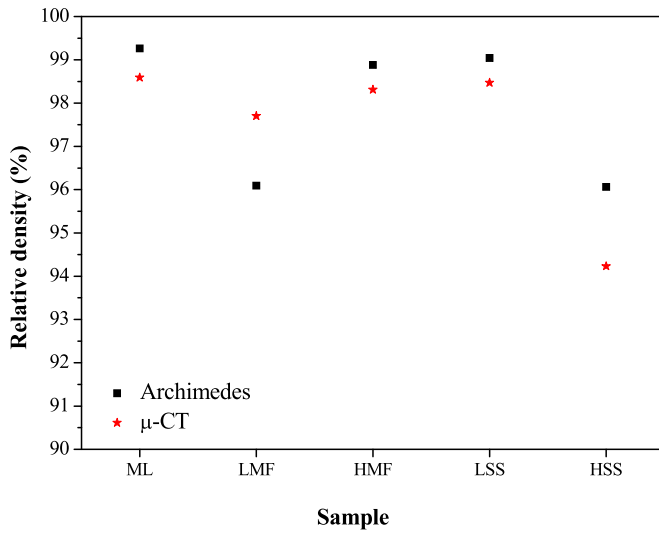


Fig. 7. Comparison between the mean relative densities of Al 5xxx deposited samples obtained from the Archimedes and μ -CT techniques.

deposited sample relative to the other reflections. A similar TOPAS analysis indicates ($R_{wp} = 9.24$) that the GA powder is comprised of 54.84 wt % pure Al, 42.33 wt% solid solution of Mg in Al, and 2.83 wt% pure Mg. This can be translated to an effective chemical composition of 95.252 wt% Al and 4.748 wt% Mg. The corresponding ICP-OES values in Table 2 are 94.645 and 4.527 wt%, respectively. Thus, there is also good agreement of the TOPAS analysis of the feedstock powder and the ICP-OES data. This further validates the reliability of the TOPAS analysis. In addition, it shows that the selective evaporation of Mg in the LENS® process can be identified also by XRD.

3.4. Microhardness

Vickers microhardness values for the as-deposited ML sample are shown in Fig. 11. A vertical (longitudinal) line scan from the top of the deposited sample down to the substrate as well as three distinct horizontal (transverse) line scans are presented in Fig. 11A,B, respectively. The overall averaged microhardness of this sample is 64.6 ± 3.6 VHN. No significant variation in hardness along the line scan is evident. A summary of the mean microhardness values of all investigated samples is presented in Fig. 11C.

3.5. Tensile test combined with DIC analysis

Uniaxial tensile tests combined with DIC analysis were carried out in order to determine the Young's modulus (E), Poisson's ratio (ν), yield stress (σ_y), ultimate tensile strength (σ_{UTS}), fracture strain (ε_f), and total strain energy density/toughness (U_T) of the as-deposited alloy. These tests were complemented by a fractography analysis. The Young's modulus was determined by linear fitting of the longitudinal stress-strain curve, whereas Poisson's ratio was determined from transverse strain-longitudinal strain curves. Both were determined in the linear-elastic region (both, for data in the range of 250–900 $\mu\epsilon$). The yield stress was determined at the 0.2% strain offset intersection with the stress-strain curve.

Fig. 12A shows engineering stress-strain curves typical of longitudinal tensile specimens. A summary of the values obtained from these tests is provided in Table 3. Although the samples were processed under different conditions of laser scan speed and powder mass flow rate, and consequently their density differs (see Fig. 3), their Poisson's ratio, yield strength, and the ultimate tensile stress values are similar. On the other hand, their fracture strain and toughness, two indicators

of ductility, seem to be more sensitive to the level of porosity, namely the ductility decreases when the density is lower.

A representative stress-strain curve is shown in Fig. 12B. A magnification of the dashed rectangular area is presented as inset. It illustrates the presence of Portevin-Le Chatelier (PLC) type-A serrations in the as-deposited Al alloy. DIC strain distribution contour images are presented in Fig. 12C. The numbers (1) through (5) correspond to the numbered points on the stress-strain curve in Fig. 12B. These images illustrate the tensile strain evolution in the direction of the applied load. It is observed that as the deformation develops, the local strain begins to increase gradually with no apparent necking at the sample's gage. At the ultimate tensile stress (point 4), necking of the sample starts to form, and localized strain concentration evolves. Point 5 illustrates the point where the fracture occurred, which indeed appears at the necking zone where the strains are maximal.

Table 4 summarizes the values of the Young's modulus, shear modulus, and Poisson's ratio deduced from pulse-echo ultrasonic tests. The rationale for conducting these tests is explained in the Supplementary file. Calculations were per Eqs. (S1)–(S3). Comparing between the values of the Young's moduli in Tables 3 and 4, it is evident that the pulse-echo ultrasonic test consistently yields higher values than DIC, although they are still somewhat lower than the value typical of wrought Al 5754-O. This difference is responsible for the slightly lower σ_y (proof stress) values reported in Table 3 based on the ultrasonic dynamic test compared to DIC. The results in Table 4 show that the shear modulus values of all samples fall within the range typical of wrought Al 5754-O, while the values of the Poisson's ratio fall within the typical range, except in the case of the LMF sample where the value is somewhat lower than the typical one.

3.6. Fracture surface morphology (fractography)

Fractography was performed in order to characterize the fracture surfaces of the tensile specimens. The analysis was focused on the two samples that exhibited the maximal and minimal toughness in tensile tests (LSS and HSS, respectively, see Table 3). Representative SEM images are shown in Fig. 13. Sample HSS is inherently more porous than sample LSS, in correspondence with the density values measured by the Archimedes method (see Figs. 3B & 7). Moreover, the majority of pores have a relatively spherical morphology. Macroscopically, the fracture surfaces of samples LSS and HSS are significantly different; LSS looks more brittle – it has a more flat surface, with macroscopically brittle features on the surface, and less pronounced shear lips. Microscopically, both fracture surfaces exhibit ductile characteristics, with fine overload dimples and apparent necking deformation. It should be emphasized that necking and fracture occurred within the gage section in all tensile specimens.

High-magnification fractography images reveal that in both samples, a small amount of irregular pores is present. Fig. 13B–D shows two faces of a non-flat area of the fracture surface with two distinct surface morphologies. The first face (marked by a green rectangle in Fig. 13B) is characterized by fine dimples, typical of ductile fracture (see Fig. 13C). The second face (marked by a red rectangle in Fig. 13B), on the other hand, reveals cleavage fracture morphology, which is typical of a more brittle fracture (see Fig. 13D).

4. Discussion

4.1. Chemical composition of the as-deposited alloy: selective evaporation of magnesium

In Section 3 it was shown that although Al 5083 powder feedstock was used, the chemical composition of the as-deposited alloy actually matches the requirements for wrought Al 5754 due to selective evaporation of Mg (and Zn) during DED. In Section 1 it was conferred that selective evaporation of elements with low boiling point (high vapor

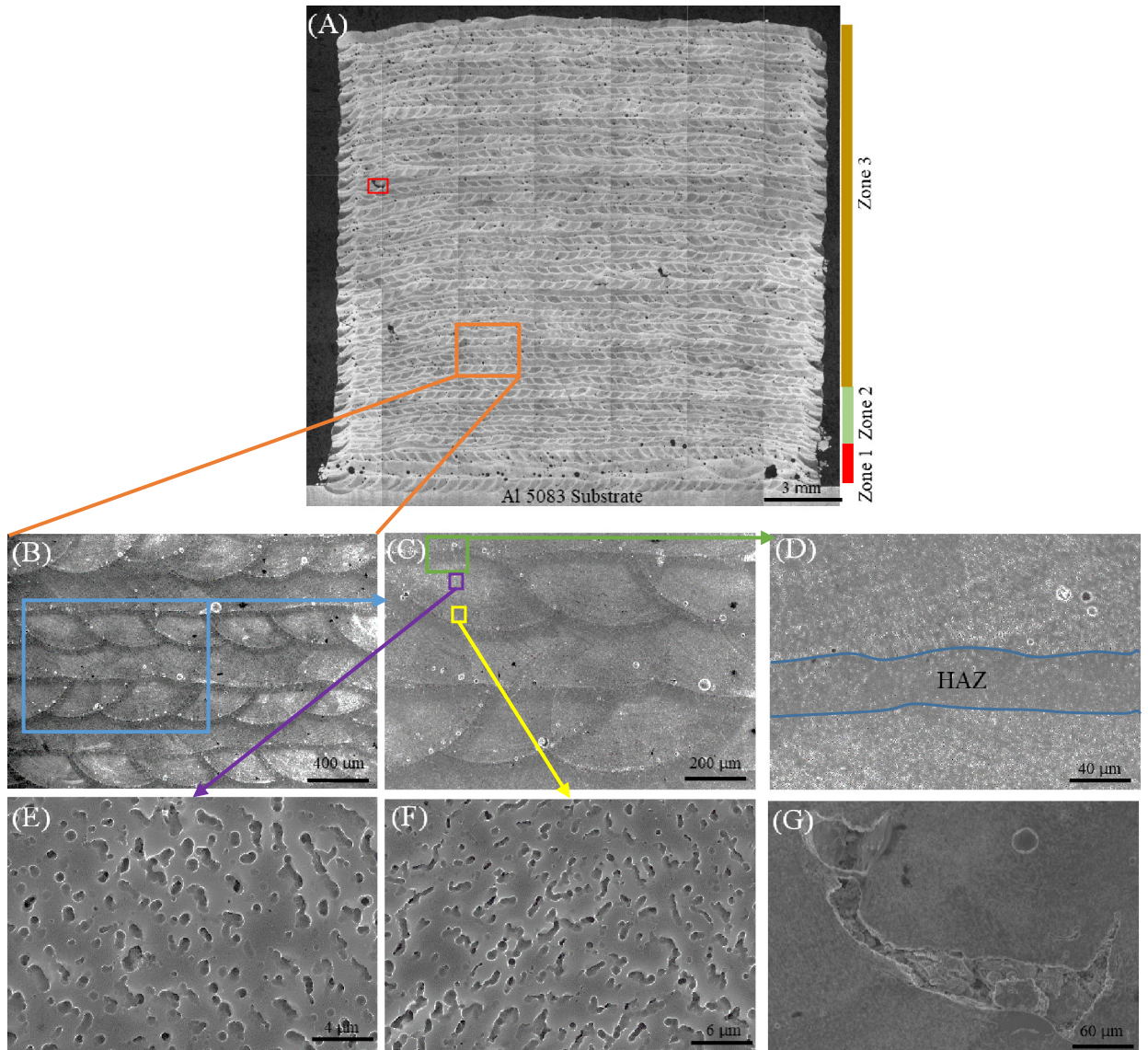


Fig. 8. (A) Light microscope composition image of the cross-section of sample ML after chemical etching. (B) SEM zoom-in image of the orange rectangle zone in (A). (C) SEM zoom-in image of the blue rectangle zone in (B). (D) SEM zoom-in image of the green rectangle zone in (C). (E) SEM zoom-in image of the purple rectangle zone in (C). (F) SEM zoom-in image of the yellow rectangle zone in (C). (G) SEM zoom-in image of the red rectangle in (A) revealing a keyhole defect due to partially-melted powder.

pressure) such as Mg [42] and Zn [43] is one of the well-known challenges in processing of high-quality structural aluminum alloys by DED as well as by PBF and laser beam welding [16,30,44–47]. This selective evaporation might result in fluctuations in alloy composition, voids and gas porosity (and, therefore, reduction in material density), degradation of mechanical properties, and hot cracking.

Interestingly, the concentration of Mg in the as-deposited alloy may somehow depend on the powder mass flow rate. From Tables 1 and 2 it is evident that while the LMF, ML and HMF samples were deposited under identical conditions of laser scan speed and energy density, as the powder mass flow rate (or, the Ar gas flow rate) is increased from 15 to 33 g/min – the concentration of Mg in the deposited alloy decreases from 2.861 to 2.628 wt%. One possible explanation is that a higher gas flow rate results in a higher flux of oxygen feed gas impurity, which reacts with Mg in its oxidation process [48]. If so, reducing the oxygen level in the build chamber to below 10 ppm (instead of 19.6–16.1 ppm used in this work), could be beneficial. It also could be that gas-dynamic phenomena [49] are responsible for the effect of the powder/argon flow rate on the evaporation of Mg. Another plausible explanation is that increase in powder mass flow rate results in a

reduction in the melt-pool temperature, which in turn reduces the amount of Mg evaporation. This, however, requires further experimental study, and is beyond the scope of this paper and deserves further study.

4.2. Density measurements: Archimedes and μ -CT analysis

The mean relative densities of the as-deposited samples measured using the Archimedes method varied between 96.06% and 99.26%, depending strongly on the processing variables. This maximal value is high compared to typical densities of alloys processed by PBF (in their *as-printed* condition), for example, and may result in mechanical properties that are similar to wrought alloys than to cast alloys.

From Figs. 3 & 7 it seems that the material density decreases as the laser scan speed is increased (or, the laser energy density is decreased) and the powder mass flow rate (or, the Ar gas flow rate) is decreased. However, based on our preliminary design of experiments (DOE), not shown herein, for both factors a “process window” was found, namely, a parabolic fit with “apparent local maximum” in the range of the process parameters better describes the dependence than a linear line fit.

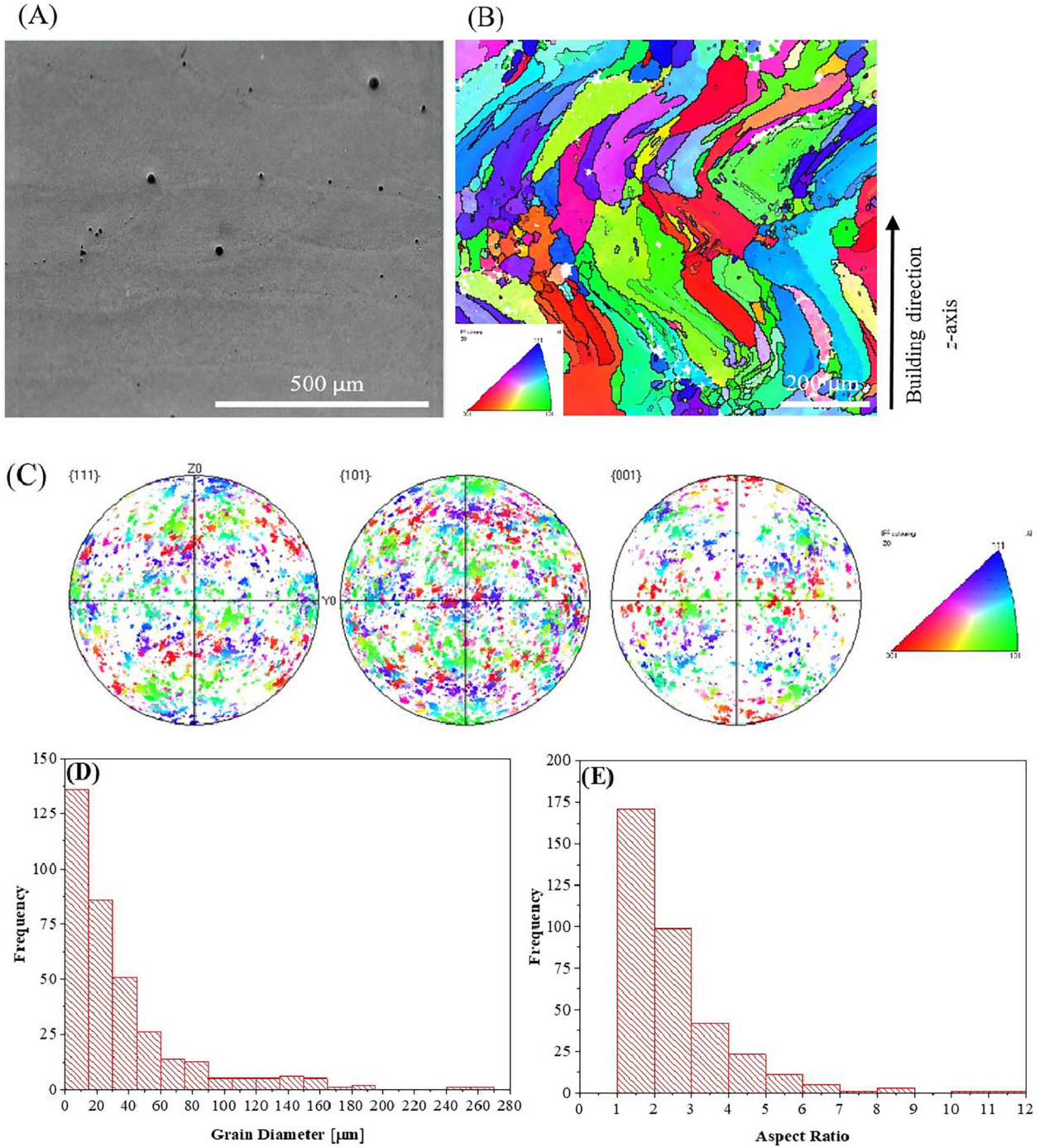


Fig. 9. (A) SEM secondary electron image of a randomly selected area in as-deposited sample ML. (B) EBSD orientation map of (A), using the inverse pole figure coloring scheme. (C) Pole figures in principle orientations $\{111\}$, $\{101\}$, and $\{001\}$. (D) Grain size distribution ($n = 357$ grains). The numeric grain size is $36.0 \pm 2.1 \mu\text{m}$. (E) Grain aspect ratio distribution ($n = 357$ grains). The numeric aspect ratio is 2.52 ± 0.08 .

In addition, Fig. 3A & B each consists of only three points, thus no local optimum can be observed, at least not within the ranges of processing parameters that were used. Therefore, one cannot claim with high certainty for a decrease in density as the scan speed is increased or the powder mass flow rate is decreased. In general, a reduction in material density of samples that were fabricated at high laser scan speed could be related to the low laser energy density and the high surface reflectivity of the Al powder, which results in insufficient melting of the powder interacting with the laser and the melt pool, and consequently – pore formation and related reduction in the observed density. On the other hand, the increase in material density of samples that were fabricated

at high powder mass flow rate could be related to the low density of the feedstock Al powder and its poor flowability, which results in unstable powder mass flow rate. The powder mass flow rate is adjusted via the Ar (carrier gas) flow rate. It should be noted that the highest density obtained was that of the ML sample, namely the sample that was deposited at middle levels for both factors (laser scan speed and powder mass flow rate). Hence, synergistic (or counter) effects of the processing parameters should be accounted for. Such effects may be revealed applying a thorough DOE methodology [50].

Several techniques are commonly used to measure the relative density and porosity of bulk materials, including AM alloys. These include

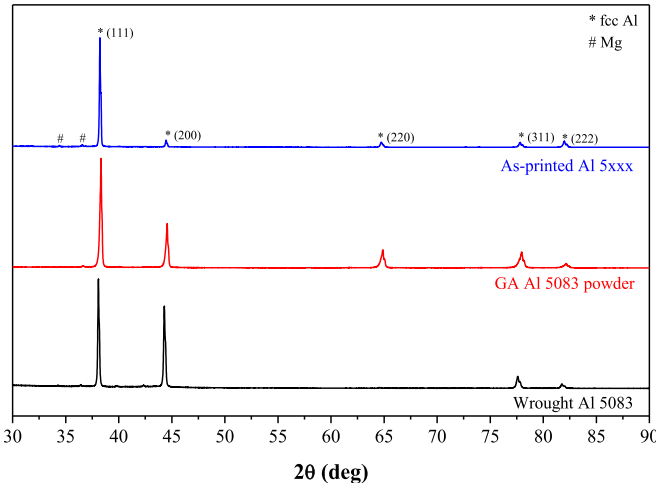


Fig. 10. XRD patterns of as-deposited Al alloy (sample ML), gas-atomized Al 5083 powder feedstock, and wrought Al 5083-O.

the Archimedes method, μ -CT, gas pycnometry, and image analysis of metallographic cross-sections [51–53]. The Archimedes method does not give any information on pore characteristics such as morphology, size, and distribution. In addition, density measurement by the Archimedes method can be influenced by surface roughness or open pores. In such cases, high surface tension of a sample does not allow the immersion fluid to completely immerse and infiltrate the analyzed sample, consequently resulting in increased density [51]. Fig. 7 shows that the relative densities measured utilizing the Archimedes method are typically higher than those obtained from μ -CT. This difference can be explained by the inherent nature of μ -CT analysis. Porosity and sphericity analysis by μ -CT can be influenced by the X-ray beam scattering that has an effect on both the achieved resolution and image artifacts [52]. In addition, the definition of image processing parameters, e.g., the threshold, can result in loss of information such as un-molten powder residues, thus possibly leading to inaccurate density values [51,53]. Finally, on one hand, due to the resolution limit of μ -CT, nanometer-size and submicron-size porosity might be overlooked in the μ -CT analysis, thus yielding a higher density value than the real one. On the other hand, porosity from the recast layer formed on samples manufactured by EDM might lower the density value in μ -CT analysis.

4.3. The origins of pores in the deposited alloy

There are various mechanisms that may lead to porosity formation during laser-based deposition of Al alloys: (1) Selective evaporation of elements with high vapor pressure, such as Mg and Zn. (2) Poor powder flowability due to the low density of the Al powder along with low viscosity of molten Al [13–16]. (3) An entrapped/dissolved gas that is present in the starting powder, which is subsequently released during DED [54]. For example, moisture absorption in the Al powder and, consequently, hydrogen-related porosity due to the significantly lower solubility in the rapidly solidified metal [7]. (4) Contamination by powder-feed gases [5]. (5) Entrapment of gases by surface turbulence and gas entrainment during turbulent impact of particles into the melt pool [5]. (6) The native oxide on the raw powder feedstock [18,19]. (7) Shrinkage [55]. (8) Collapse of unstable keyholes [56–58].

The porosity in the samples is evident in Figs. 2 (SEM image of cross-section), 3 & 8A (optical micrographs), 4–6 (μ -CT), and 13 (SEM image of a fracture surface). Spherical pores were observed scattered throughout the deposited samples; given their morphology, they likely represent gas porosity. We hypothesized that if the pores originated from the selective evaporation of Mg, then residual Mg should be present at the inner wall of the pores. However, EDS line-scan analysis across

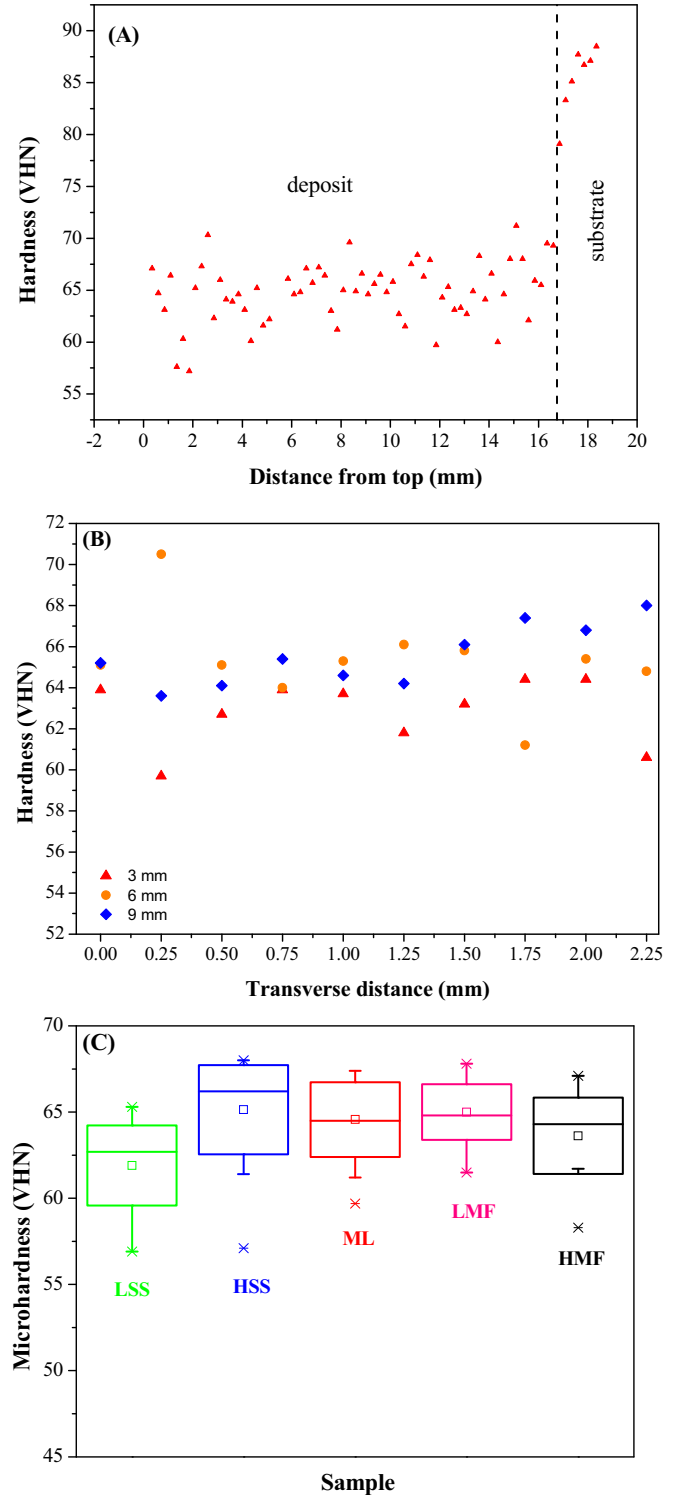


Fig. 11. Vickers microhardness measurements on the as-deposited ML sample. (A) Discrete vertical line scan from the top of the sample to the substrate. (B) Discrete transverse line scans at various deposition heights (distance is given from the top of the sample). The measured Vickers microhardness values at distances of 3, 6, and 9 mm were 62.8 ± 1.5 , 65.3 ± 2.2 , and 65.5 ± 1.4 VHN, respectively. (C) A summary of the hardness measurements of the as-deposited Al samples.

random spherical pores in metallographic cross-sections did not reveal accumulation of Mg at the pore surface (Fig. 2). Therefore, within the resolution constraints of the EDS line-scan measurements, it appears unlikely that the elemental evaporation of Mg was the principal cause of the observed porosity. From Table 1 and Figs. 3 & 7 it may seem

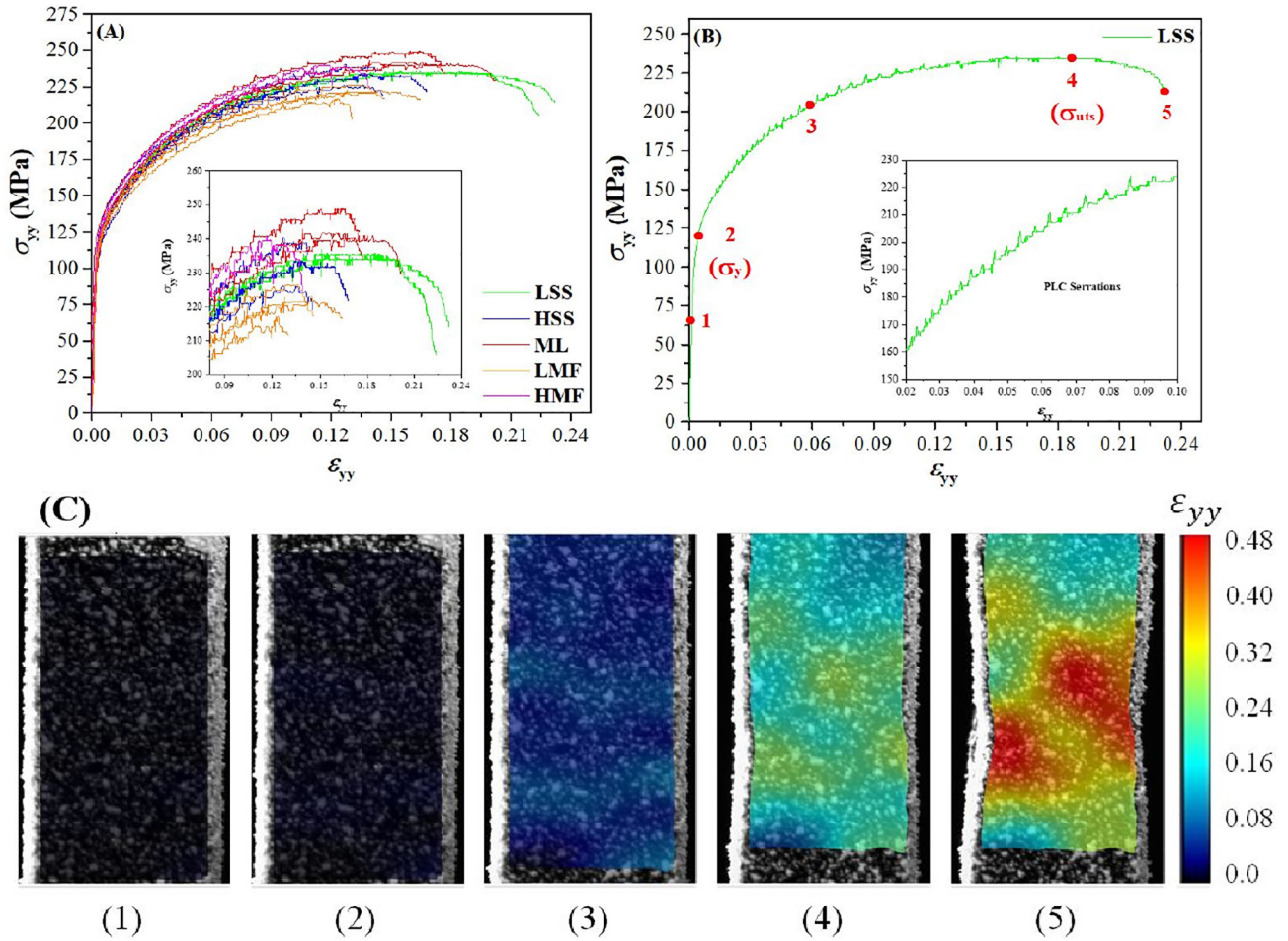


Fig. 12. (A) Engineering stress-strain curves of all as-deposited Al samples. (B) A representative stress-strain curve. The inset shows PLC serrations. (C) DIC longitudinal strain-contour images corresponding to the numbered points along the stress-strain curve presented in (B). Initial gage dimensions of the tensile sample are shown in Fig. 1B.

that the material density increased as the powder mass flow rate (or, Ar flow rate) was increased. If so, Ar gas entrapment during the rapid solidification is unlikely to be a principal cause of the observed porosity either. However, the reservations raised in the Section “Density measurements: Archimedes and μ -CT analysis” should be borne in mind. On the other hand, due to the same effect of powder mass flow rate on the material density, the poor Al powder flowability may be one of the main contributors to porosity formation. In another study where porosity was found to increase with an increase in powder mass flow [59], it was argued that a higher powder density in the powder gas jet results in more hollow particles injected to the process, and therefore, a higher possibility of process gas entrapment in the process. In addition, the laser energy may not be efficient to melt all the powder injected. Yet, hydrogen gas precipitation may be a more significant

Table 4
Elastic constants of the deposited alloy based on the pulse-echo ultrasonic test.

	E (GPa)	G (GPa)	v
LSS	68.1	25.5	0.337
HSS	66.6	25.1	0.330
ML	68.4	25.6	0.337
LMF	65.0	24.5	0.324
HMF	68.1	25.5	0.337
Wrought Al 5754-O	69–71 ^a	23–27 ^b	0.33–0.34 ^b

^a Ref. [36].

^b CES EduPack 2018, Granta Design, Cambridge, UK.

Table 3

Mechanical properties of deposited samples based on tensile tests with DIC analysis.

	E (GPa)	$\sigma_{y,DIC}^a$ (MPa)	$\sigma_{y,NDT}^b$ (MPa)	σ_{UTS} (MPa)	ϵ_f (%)	v	U_T (J/mm ³)
LSS	62.0 ± 2.7	119.3 ± 2.5	117.4 ± 3.5	233.2 ± 3.5	18.9 ± 5.6	0.33 ± 0.06	39.7 ± 12.4
HSS	61.8 ± 3.9	115.0 ± 4.6	112.7 ± 4.0	226.0 ± 5.0	13.8 ± 2.7	0.32 ± 0.04	26.9 ± 6.2
ML	62.5 ± 1.3	121.4 ± 4.7	119.8 ± 4.7	244.3 ± 3.4	18.3 ± 1.0	0.32 ± 0.02	39.7 ± 2.1
LMF	63.0 ± 2.0	117.0 ± 3.0	116.6 ± 2.4	221.9 ± 3.3	14.8 ± 1.1	0.33 ± 0.03	38.9 ± 2.4
HMF	65.7 ± 2.5	121.0 ± 0.4	119.6 ± 2.0	239.0 ± 0.6	16.9 ± 4.0	0.34 ± 0.01	27.1 ± 2.7
Wrought Al 5754-O [35]	69–71	Min 80	Min 80	190–240	Min 16% ^c	0.33–0.34 ^d	–

^a Proof stress from the engineering stress-strain curve, using the value of E obtained from DIC.

^b Proof stress from the engineering stress-strain curve, using the value of E obtained from the ultrasonic dynamic test.

^c For specimen thickness 1.5–3.0 mm. The specimen thickness in this study was 2.0 mm.

^d CES EduPack 2018, Granta Design, Cambridge, UK.

contributor to porosity formation in this work. The source of this hydrogen could be either moisture absorption in the Al powder, which was not baked before DED, or contamination by the Ar powder-feed gas. Hydrogen concentration analysis, either of the bulk material or better locally around pores by techniques such as atom probe tomography (APT) [60] or secondary ion mass spectrometry (SIMS) [61], is still to be conducted in order to validate this hypothesis.

Porosity such as in Fig. 8G is related to lack of fusion, where inclusions of un-melted particles are entrapped in between the unbounded surfaces. Such defects often originate from insufficient laser melting at the interlayer boundaries during processing [62]. In addition, porosity due to lack of fusion may arise from rapid cooling and melt-pool instability due to the high thermal dissipation through the deposited Al alloy and the Al alloy substrate [63], or from the native oxide on the raw powder feedstock. Finally, the inherent porosity of the powder feedstock due to the gas atomization process may be responsible to some of the interlayer porosity in the as-deposited material [64].

4.4. The microstructure of the as-deposited alloy

The microstructure of the as-deposited alloy is reflected in Figs. 8B–G (SEM cross-section images), 9 (EBSD analysis), and 10 (XRD patterns). The entire deposit consists of a mesh-like morphology, with an inter-pass HAZ from thermal heating during successive layer depositions [34]. The metal flow trails and inter-pass boundaries appear to be well fused throughout the deposited sample. This can be related to epitaxial interfaces [34]. No evidence of hot cracking is observed. The as-deposited microstructure consists of both columnar and equiaxed grains. This growth orientation is affected by the laser scan direction, and is therefore related to the heat flux direction across the melt pool [65]. This result is consistent with previous reports that show similar grain growth when using a similar deposition strategy in DED [34,66]. Rietveld refinement indicates that the as-deposited alloy is comprised of 94.55 wt% pure fcc Al, 2.62 wt% solid solution of Mg in Al, and 2.83 wt% pure Mg. The XRD-TOPAS analysis is consistent with the SEM images, according to which the as-deposited alloy is comprised of a minor amount of Mg-rich phase surrounded by an Al matrix. Since pure Mg seems to exist already in the feedstock powder, its identification in the as-deposited alloy excludes the option that its origin is selective evaporation and consolidation during the LENS® process. It should also be noted that in the Al-Mg phase diagram, no phase separation to either pure Al or pure Mg exists (namely, Al and Mg both have solid solutions in which the other element is dissolved). Therefore, the formation of both pure Al and pure Mg is a non-equilibrium process, or results from fast kinetics. The XRD results are also in good agreement with the EBSD analysis with respect to the crystallographic orientation. Fig. 8E,F reveals some differences in the microstructure in two distinct zones in a single solidification cell, which can be explained by variations in the local cooling rates and heat dissipation during the solidification process [67].

4.5. Mechanical behavior of the 3D printed aluminum alloy

The mean value of the hardness of the as-deposited Al alloy (Fig. 11) is substantially lower than the nominal Vickers microhardness of the Al 5083 substrate (83.7 ± 2.6 VHN). This difference can be explained by the selective evaporation of Mg – the main strengthening element in this alloy – during the laser deposition process. As shown in Table 2 and discussed above, the chemical composition of the as-deposited alloy is most similar to that of wrought Al 5754. Yet, the hardness of the as-deposited alloy is slightly higher than that of Al 5754-O (52 BHN [36] ≈ 58 VHN). This is consistent with various reports showing that the refined grains resulting from the LENS® process result in increased microhardness [14,66].

Table 3 shows that all as-deposited samples have Young's modulus values that are somewhat lower than that typical of wrought Al 5xxx

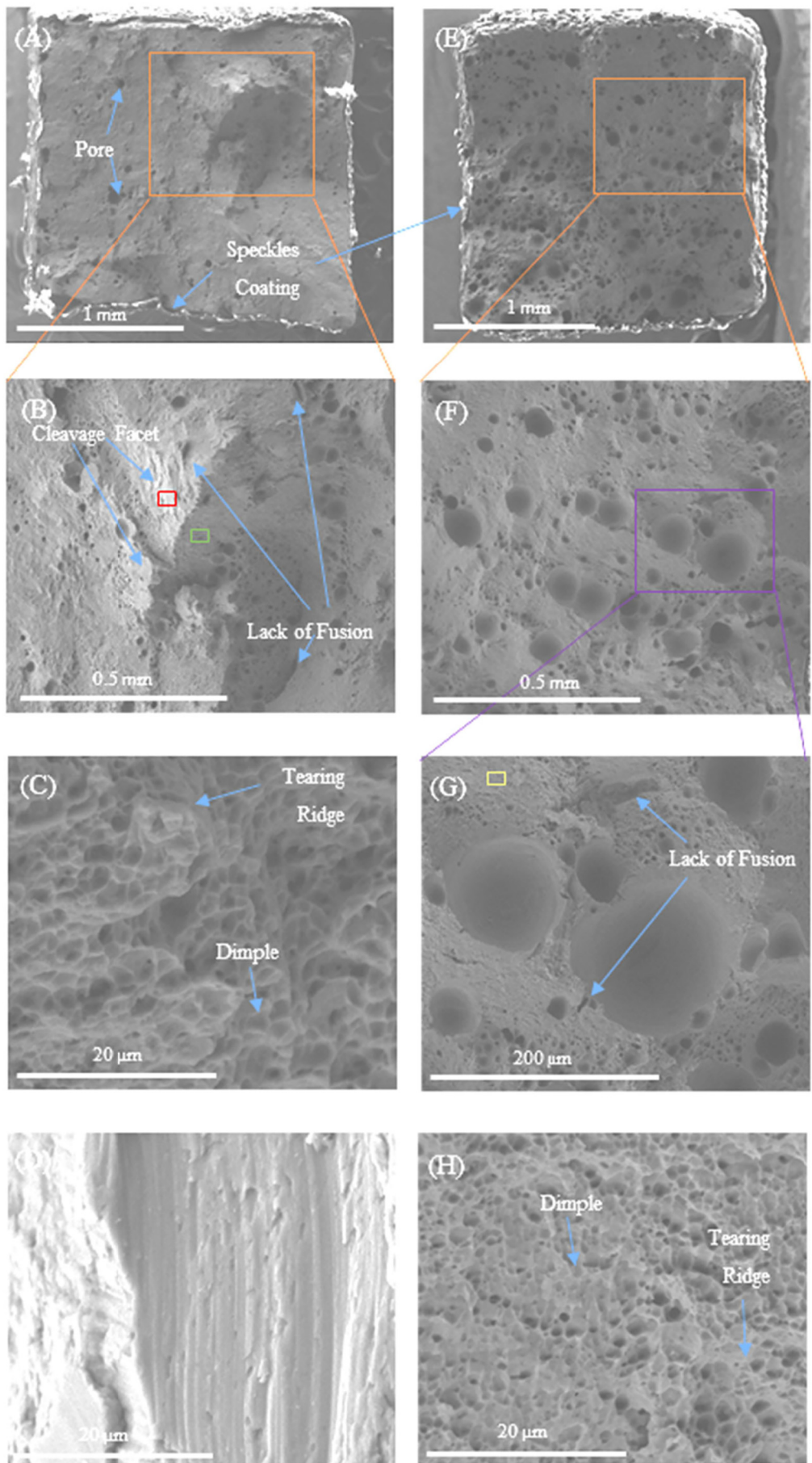
alloys [40]. This is likely due to the presence of porosity in the as-deposited samples. A correlation has been reported between the value of the Young's modulus and the level of porosity, and several theories and formulae have been suggested to describe this relationship [68–72]. In spite of the porosity, the values of the yield strength, ultimate tensile strength, and elongation at break of the LSS and HMF samples all meet the requirements of the ISO-BS-EN 485-2:2016 standard [36] for wrought Al 5754-O. There is good agreement between the ductility values obtained from DIC analysis and the hardness results, namely, lower ductility corresponds to higher hardness, and vice versa. HMF has higher E value, while LSS has higher U_T value. Hence, the preference of one over the other with respect to mechanical properties would depend on the design criterion (rigidity vs. toughness). Further DOE for process optimization is likely to result in a material with reduced porosity and even better mechanical properties.

Fig. 12 shows PLC type-A serrations in the stress-strain curve of the as-deposited Al alloy. Both AM and wrought Al-Mg alloys (e.g., the 5xxx series, including Al 5754-O) often fail by plastic flow localization into narrow shear bands, and not by the classical ductile fracture [73,74]. Depending on the appearance of the serrations in the stress-strain curve during constant strain rate tensile tests, the PLC bands are classified as types A, B, and C [73]. Type A is associated with the highest strain rate and/or lowest temperature. The PLC effect is the outcome of dynamic strain aging of the alloy due to interaction between solute Mg atoms and mobile dislocations [74]. The PLC effect leads to changes in the mechanical behavior of the material, such as strength increase and ductility decrease [73,74].

There seems to be good correspondence between the tensile test results (Fig. 12) and the microhardness results. Increase in hardness is usually associated with decrease in ductility, and vice versa. Here, sample LSS that has the highest ductility among all deposited materials (see Table 3) also has the lowest microhardness (see Fig. 11C).

Comparing the values of density based on the Archimedes test (Fig. 7), the E -values based on DIC (Table 3), and the values of E based on the ultrasonic test (Table 4), there is a one-to-one correlation between the order of density (or, porosity) values and the order of E -values based on the ultrasonic test, which does not exist in the case of DIC-based E -values. This is possibly because the ultrasonic test measures through-specimen properties, whereas DIC monitors the outer surface of the specimen. This further supports our recommendation to use dynamic tests such as the pulse-echo ultrasonic test for measurement of the elastic constants of AM alloys, in addition to tensile tests combined with DIC. It should be noted that the tensile test specimens that we used were smaller than standard ones, and that the CCD digital cameras were 5 MP, 12-bit. Using larger samples with high-resolution cameras would probably increase the accuracy of the DIC analysis. It should be borne in mind that the “dynamic” wave measurements yield a total average of the wave speed over time (and, thus, space). In contrast, DIC is a full-field technique where the values extracted do depend on the spatial distribution and window size. It should also be noted that the presumably switched order of the E -values of the LMF and HSS samples by ultrasonic test measurements is related to the use of thin samples for these measurements, which might not represent statistically the effective density of the sample. For example, the density values of the samples used for the ultrasonic tests were 2.637, 2.631, 2.629, 2.611, and 2.554 g/cm³ for the ML, LSS, HMF, HSS, and LMF samples, respectively. This problem, however, could easily be overcome by increasing the number of samples used for ultrasonic tests.

From Fig. 13 (SEM fractography) it is clear that sample HSS is inherently more porous than sample LSS, in correspondence with the density values measured by the Archimedes method (see Fig. 7). Moreover, the majority of pores have a relatively spherical morphology. This observation is consistent with the μ -CT sphericity analysis (see Figs. 4 & 6 and related text). High-magnification fractography images reveal that in both samples, a small amount of irregular pores is present, most likely due to lack of fusion between adjacent tracks during deposition. The



fractography SEM images together with the mechanical properties reported above indicate that the inherent porosity has a detrimental effect on the observed tensile properties. Future AM process optimization is still needed in order to improve the physical and mechanical properties.

The mixed type of fracture mechanisms evident in Fig. 13B–D is frequently termed “quasi-cleavage” [75]. This type of fracture can be explained by the nucleation and propagation of a crack through a critical lack of fusion defect along a cleavage plane of the neighboring grain. Propagation of the formed crack proceeds through neighboring grains across the as-deposited Al, until final fracture takes place [76,77].

4.6. Potential applications and further alloy modification

One could argue what the benefit of AM of an alloy such as Al 5754-O is. This last Section is aimed at answering this question. Wrought Al 5754 has mid-strength, excellent corrosion resistance, good weldability, very good burnishing and anodizing quality, and very good plasticity in its soft condition. One may argue that in the aircraft industry, the largest user of and investor in AM, non-heat-treatable alloys such as Al 5754 are of less interest. While this is true, the potential markets for this alloy are still sufficiently large. Current applications of Al 5754 include shipbuilding, automobile manufacturing (in the sheet form, and at different temper conditions, it is the main material used to manufacture vehicle frames, seals, etc.), buses, railway and underground wagons, food processing equipment, welded chemical and nuclear structures, storage tanks, boiler-making, recipients for petrol, architecture and interior design, fishing industry equipment, treadplates, fridges, beverage cans, etc. Al 5754 has been widely used in sports and high-end cars like Jaguar XK, Lotus Evora, Chevrolet Corvette [78], and BMW 7 [79]. A second argument could be that since aluminum alloys are relatively easy and cheap to process, and since DED is limited in the geometric complexities that it can print, DED of an aluminum alloy such as Al 5754 may not be economically attractive. However, wrought Al 5754 suffers from some manufacturability limitations that may make manufacturing Al 5754 parts by DED attractive. Due to the high resistance of Al 5754 to hot forming, the manufacturing of real parts is limited to simple section geometries. A third criticism could be that if the mechanical properties of a non-heat-treatable alloy in its as-deposited conditions are similar to those of the wrought alloy in the annealed condition, and since post-printing work-hardening might be complicated, expensive, or even not possible, then it does not make sense to print such alloys. Furthermore, since its cutting tool suitability is low in the soft temper, and in order to increase its strength, the wrought material is often used in a work-hardened temper – mainly H22 (work-hardened by rolling and then annealed to 1/4 hard). However, Al 5754 has many applications in the annealed condition! For example, in its plate form, Al 5754 is often used in the annealed temper. Furthermore, according to The Aluminum Association, Inc. [80], “automotive structures are likely to employ increasing amounts of Al 5754-O for parts such as internal door stiffeners or the entire body-in-white.” Finally, a significant benefit of AM of Al 5754-O could be the ability to transform it quite easily to a heat-treatable alloy with improved mechanical properties by minor alloying in the 3D printing stage. Addition of small quantities of scandium (Sc) – currently as low as 50–75 at. ppm – has been a common approach toward improving the strength and recrystallization resistance of 5xxx aluminum alloys. Upon aging, coherent nanometer-size Al_3Sc precipitates form, with a high stability up to the melting temperature of Al [80]. Zr is added to improve the thermal stability of Al_3Sc precipitates and to decrease the price of the alloying additions [81]. Seidman et al. [81] modified Al 5754 alloy with small quantities of Sc and Zr. The tensile strength of the modified alloy was higher than that of Sc-

and Zr-free Al 5754-O alloy. Recently, Zhou et al. [82] manufactured by SLM a heat-treatable Al–6Zn–2 Mg alloy with 1 wt% (Sc + Zr). Alloying with Sc and Zr promoted the formation of $\text{Al}_3(\text{Sc},\text{Zr})$ precipitates, which contributed to grain refinement and enhanced tensile properties. Thus, an interesting future direction could be to add little Sc, Zr, erbium (Er) and some other elements to the Al 5083 powder that was used in this study, 3D print it with LENS® (which allows obtaining fine microstructures with enhanced mechanical properties), and post heat-treat it (unless found unnecessary) to form fine precipitates, thus obtaining a modified Al 5754-O alloy with enhanced mechanical properties.

5. Conclusions

In this paper, we describe the DED of Al 5xxx alloy by LENS®. The effects of processing parameters such as powder mass flow rate and laser scan speed on the chemical composition, density, and mechanical properties of the deposited material are discussed. The main conclusions drawn are as follows:

- 1) Although Al 5083 gas atomized powder feedstock was used, the chemical composition of the as-deposited alloy is as that of wrought Al 5754, due to selective evaporation of Mg (and Zn) during deposition.
- 2) The microstructure of the as-deposited alloy is comprised of a small amount of pure Mg hcp phase surrounded by a matrix of fcc Al phase. The microstructure consists of both equiaxed and columnar grains. Neither preferred crystallographic orientation nor hot cracking is evident.
- 3) The mean relative densities of the as-deposited samples vary between 96.06% and 99.26%, depending strongly on the processing variables. The material density seems to decrease as either the laser scan speed is increased or the powder mass flow rate is decreased. The best densities achieved are high compared to typical densities of alloys processed by PBF, at least in their as-deposited condition. Various mechanisms could contribute to porosity formation in the DED of the Al 5754 alloy, gas-related porosity being the major one.
- 4) No significant variation in microhardness is observed along the deposition direction (z -axis). Despite some porosity, combinations of process parameters have been identified that yield deposits which satisfy the requirements of international standards or material specifications for static mechanical properties of wrought Al 5754-O. The pulse-echo ultrasonic test is found to yield more accurate values of the Young's modulus than the tensile test combined with DIC analysis, and consistently yields higher Young's modulus values. The fracture surfaces are of ductile nature.
- 5) Further DOE is likely to result in a material with reduced porosity and even better mechanical behavior. DED of Al 5754-O has many potential applications and markets by itself. In addition, by alloying the powder feedstock with small quantities of Sc, Zr, Er, and some other elements, a heat-treatable alloy with enhanced mechanical properties may be processed by LENS® DED. This study lays the foundation for further exploration into AM of Al 5xxx alloys by DED.

CRedit authorship contribution statement

David Svetlizky: Conceptualization, Methodology, Investigation, Data curation, Writing - original draft, Visualization. **Baolong Zheng:** Methodology, Investigation, Writing - review & editing. **Tali Buta:** Investigation, Writing - review & editing, Visualization. **Yizhang Zhou:**

Fig. 13. SEM-SE images of fracture surfaces after tension tests. (A–D) Sample LSS. (E–H) Sample HSS. The magnification gradually increases from top to bottom, with each color rectangle shown at higher magnification in the image below.

Methodology, Writing - review & editing. **Oz Golan:** Investigation, Data curation, Writing - review & editing, Visualization. **Uri Breiman:** Investigation, Writing - review & editing. **Rami Haj-Ali:** Resources, Writing - review & editing, Supervision. **Julie M. Schoenung:** Conceptualization, Methodology, Resources, Writing - review & editing, Supervision, Funding acquisition. **Enrique J. Lavernia:** Conceptualization, Methodology, Resources, Writing - review & editing, Supervision, Funding acquisition. **Noam Eliaz:** Conceptualization, Methodology, Resources, Data curation, Writing - original draft, Writing - review & editing, Visualization, Supervision, Project administration, Funding acquisition.

Declaration of competing interest

The authors declare that they have no known competing financial interests or personal relationships that could have appeared to influence the work reported in this paper.

Acknowledgements

The authors thank Dr. Victor Fourman, Mr. Eliran Hamo, Dr. Zahava Barkay from the Wolfson Applied Materials Research Center at Tel-Aviv University, Dr. Eli Brosh from NRCN, Mr. David Noiman from NRCN, and Mr. Nadav Guy from NRCN for their technical assistance in tensile tests with DIC analysis, XRD measurements, ESEM-EBSD characterization, pulse-echo ultrasonic tests, Archimedes density measurements of the samples for these ultrasonic tests, and oxygen analysis, respectively. The team at UCI is grateful to the Israel Ministry of Defense for its financial support under P.O. No. 4440873734.

Appendix A. Supplementary data

Supplementary data to this article can be found online at <https://doi.org/10.1016/j.matdes.2020.108763>.

References

- [1] S.M. Thompson, L. Bian, N. Shamsaei, A. Yadollahi, An overview of direct laser deposition for additive manufacturing; part I: transport phenomena, modeling and diagnostics, *Addit. Manuf.* 8 (2015) 36–62, <https://doi.org/10.1016/j.addma.2015.07.001>.
- [2] Z.Y. Liu, C. Li, X.Y. Fang, Y.B. Guo, Energy consumption in additive manufacturing of metal parts, *Proced. Manuf.* 26 (2018) 834–845, <https://doi.org/10.1016/j.promfg.2018.07.104>.
- [3] F.A. España, V.K. Balla, A. Bandyopadhyay, Laser processing of bulk Al–12Si alloy: influence of microstructure on thermal properties, *Philos. Mag.* 91 (2011) 574–588, <https://doi.org/10.1080/14786435.2010.526650>.
- [4] N. Ramesh, Structure-Process-Property Relationships for LENS® and SLM Processed AlSi10Mg Alloys and the Effect of Heat Treatment, MSc Dissertation University of California, Irvine, 2018.
- [5] B. Zheng, Y. Li, J.E. Smugeresky, Y. Zhou, D. Baker, E.J. Lavernia, Hybrid Al + Al3Ni metallic foams synthesized in situ via laser engineered net shaping, *Philos. Mag.* 91 (2011) 3473–3497, <https://doi.org/10.1080/14786435.2011.586375>.
- [6] H.A. Macleod, *Thin Film Optical Filters*, 4th edition CRC Press, Boca Raton, FL, 2010 185–196.
- [7] J. Zhang, B. Song, Q. Wei, D. Bourell, Y. Shi, A review of selective laser melting of aluminum alloys: processing, microstructure, property and developing trends, *J. Mater. Sci. Technol.* 35 (2019) 270–284, <https://doi.org/10.1016/j.jmst.2018.09.004>.
- [8] Y.S. Touloukian, D.P. DeWitt (Eds.), *Thermophysical Properties of Materials, Thermal Radiative Properties-Metallic Elements and Alloys*, 7, IFI/Plenum, New York, NY, 1970.
- [9] I. Polmear, D. Stjohn, J.-F. Nie, M. Qian, *Light Alloys: Metallurgy of the Light Metals*, 5th edition Elsevier, Oxford, UK, 2017.
- [10] M.L. Baucio (Ed.), *ASM Metals Reference Book*, 3rd edition ASM International, USA, 1993.
- [11] M. Boivineau, C. Cagran, D. Doytier, V. Eyraud, M.H. Nadal, B. Wilthan, G. Pottlacher, Thermophysical properties of solid and liquid Ti–6Al–4V (TA6V) alloy, *Int. J. Thermophys.* 27 (2006) 507–529, <https://doi.org/10.1007/PL00021868>.
- [12] W.H. Hosford, *Physical Metallurgy*, 2nd edition CRC Press, Boca Raton, FL, 2010.
- [13] J.C. Ion, *Laser Processing of Engineering Materials: Principles, Procedure and Industrial Application*, Elsevier Butterworth-Heinemann, Oxford, UK, 2005.
- [14] K. Kempen, L. Thijss, J. Van Humbeeck, J.-P. Kruth, Processing AlSi10Mg by selective laser melting: parameter optimisation and material characterisation, *Mater. Sci. Technol.* 31 (2015) 917–923, <https://doi.org/10.1179/1743284714Y.0000000702>.
- [15] N.T. Aboulkhair, Additive Manufacture of an Aluminium Alloy: Processing, Microstructure, and Mechanical Properties, PhD Dissertation University of Nottingham, UK, 2016.
- [16] Y. Ding, J.A. Muñiz-Lerma, M. Trask, S. Chou, A. Walker, M. Brochu, Microstructure and mechanical property considerations in additive manufacturing of aluminum alloys, *MRS Bull.* 41 (2016) 745–751, <https://doi.org/10.1557/mrs.2016.214>.
- [17] E.O. Olakanmi, Selective laser sintering/melting (SLS/SLM) of pure Al, Al–Mg, and Al–Si powders: effect of processing conditions and powder properties, *J. Mater. Process. Technol.* 213 (2013) 1387–1405, <https://doi.org/10.1016/j.jmatprot.2013.03.009>.
- [18] L. Thijss, K. Kempen, J.-P. Kruth, J. Van Humbeeck, Fine-structured aluminium products with controllable texture by selective laser melting of prealloyed AlSi10Mg powder, *Acta Mater.* 61 (2013) 1809–1819, <https://doi.org/10.1016/j.actamat.2012.11.052>.
- [19] E. Louis, P. Fox, C.J. Sutcliffe, Selective laser melting of aluminium components, *J. Mater. Process. Technol.* 211 (2011) 275–284, <https://doi.org/10.1016/j.jmatprot.2010.09.019>.
- [20] G.P. Dinda, A.K. Dasgupta, S. Bhattacharya, H. Natu, B. Dutta, J. Mazumder, Microstructural characterization of laser-deposited Al 4047 alloy, *Mater. Mater. Trans. A* 44 (2013) 2233–2242, <https://doi.org/10.1007/s11661-012-1560-3>.
- [21] S. Zhang, P. Ma, Y. Jia, Z. Yu, R. Sokkalingam, X. Shi, P. Ji, J. Eckert, K.G. Prashanth, Microstructure and mechanical properties of Al–(12–20) Si Bi-material fabricated by selective laser melting, *Materials* 12 (2019) 2126, <https://doi.org/10.3390/ma12132126>.
- [22] K.G. Prashanth, S. Scudino, H.J. Klauss, K.B. Surreddi, L. Löber, Z. Wang, A.K. Chaubey, U. Kühn, J. Eckert, Microstructure and mechanical properties of Al–12Si produced by selective laser melting: effect of heat treatment, *Mater. Sci. Eng. A* 590 (2014) 153–160, <https://doi.org/10.1016/j.msea.2013.10.023>.
- [23] X.J. Wang, L.C. Zhang, M.H. Fang, T.B. Sercombe, The effect of atmosphere on the structure and properties of a selective laser melted Al–12Si alloy, *Mater. Sci. Eng. A* 597 (2014) 370–375, <https://doi.org/10.1016/j.msea.2014.01.012>.
- [24] A. Singh, A. Ramakrishnan, G. Dinda, Fabrication of Al–11.2Si components by direct laser metal deposition for automotive applications, *J. Korean Weld. Join. Soc.* 35 (2017) 67–73, <https://doi.org/10.5781/JWJ.2017.35.4.10>.
- [25] M. Javidani, J. Arreguin-Zavalá, J. Danovitch, Y. Tian, M. Brochu, Additive manufacturing of AlSi10Mg alloy using direct energy deposition: microstructure and hardness characterization, *J. Therm. Spray Tech.* 26 (2017) 587–597, <https://doi.org/10.1007/s11666-016-0495-4>.
- [26] Y.J. Liu, Z. Liu, Y. Jiang, G.W. Wang, Y. Yang, L.C. Zhang, Gradient in microstructure and mechanical property of selective laser melted AlSi10Mg, *J. Alloys Compd.* 735 (2018) 1414–1421, <https://doi.org/10.1016/j.jallcom.2017.11.020>.
- [27] F. Calignano, D. Manfredi, E.P. Ambrosio, L. Iuliano, P. Fino, Influence of process parameters on surface roughness of aluminum parts produced by DMLS, *Int. J. Adv. Manuf. Technol.* 67 (2013) 2743–2751, <https://doi.org/10.1007/s00170-012-4688-9>.
- [28] N.D. Alexopoulos, S.G. Pantelakis, Quality evaluation of A357 cast aluminum alloy specimens subjected to different artificial aging treatment, *Mater. Des.* 25 (2004) 419–430, <https://doi.org/10.1016/j.matdes.2003.11.007>.
- [29] H. Ye, An overview of the development of Al–Si-alloy based material for engine applications, *J. Mater. Eng. Perform.* 12 (2003) 288–297, <https://doi.org/10.1361/105994903770343132>.
- [30] A. Mauduit, S. Pillot, H. Gransac, Study of the suitability of aluminum alloys for additive manufacturing by laser powder-bed fusion, *U.P.B. Sci. Bull., Ser. B* 79 (2017) 219–238.
- [31] L. Zhou, H. Hyer, S. Park, H. Pan, Y. Bai, K.P. Rice, Y. Sohn, Microstructure and mechanical properties of Zr-modified aluminum alloy 5083 manufactured by laser powder bed fusion, *Addt. Manufact.* 28 (2019) 485–496, <https://doi.org/10.1016/j.addma.2019.05.027>.
- [32] S. Bathula, R.C. Anandani, A. Dhar, A.K. Srivastava, Microstructural features and mechanical properties of Al 5083/SiCp metal matrix nanocomposites produced by high energy ball milling and spark plasma sintering, *Mater. Sci. Eng. A* 545 (2012) 97–102, <https://doi.org/10.1016/j.msea.2012.02.095>.
- [33] N. Eliaz, D. Svetilzky, J. Schoenung, E. Lavernia, Y. Zhou, B. Zheng, Deposition of Al 5xxx Alloy Using Laser Engineered Net Shaping, US Provisional Patent Application 62/948, 354, Filed December 16, 2019.
- [34] N. Yang, J. Yee, B. Zheng, K. Gaiser, T. Reynolds, L. Clemon, W.Y. Lu, J.M. Schoenung, E.J. Lavernia, Process-structure-property relationships for 316L stainless steel fabricated by additive manufacturing and its implication for component engineering, *J. Therm. Spray Technol.* 26 (2017) 610–626, <https://doi.org/10.1007/s11666-016-0480-y>.
- [35] J. Mazumder, A. Schifferer, J. Choi, Direct materials deposition: designed macro and microstructure, *Mater. Res. Innov.* 3 (1999) 118–131, <https://doi.org/10.1007/s100190050137>.
- [36] BS EN 485-2, *Aluminum and Aluminium Alloys - Sheet, Strip and Plate Part 2: Mechanical Properties*, 2016, British Standards Institution, London, UK, 2016.
- [37] R. Haj-Ali, R. Elias, V. Fourman, C. Tzur, G. Bar, E. Grossman, R. Verker, R. Gvishi, I. Gouzman, N. Eliaz, Mechanical characterization of aerogel materials with digital image correlation, *Microporous Mesoporous Mater.* 226 (2016) 44–52, <https://doi.org/10.1016/j.micromeso.2015.12.035>.
- [38] E. Ingram, O. Golan, R. Haj-Ali, N. Eliaz, The effect of localized vibration during welding on the microstructure and mechanical behavior of steel welds, *Materials* 12 (2019), 2553, <https://doi.org/10.3390/ma12162553>.
- [39] T. Sol, S. Hayun, D. Noiman, E. Tiferet, O. Yesheskel, O. Tevet, Nondestructive ultrasonic evaluation of additively manufactured AlSi10Mg samples, *Addit. Manufact.* 22 (2018) 700–707, <https://doi.org/10.1016/j.addma.2018.06.016>.

- [40] R.B.C. Cayless, Alloy and temper designation systems for aluminum and aluminum alloys, ASM Handbook, Vol. 2: Properties and Selection: Nonferrous Alloys and Special-purpose Materials, ASM International, Materials Park, OH 1990, pp. 15–28, <https://doi.org/10.1361/asmhba0001058>.
- [41] ASTM B209 – 14, Standard Specification for Aluminum and Aluminum-alloy Sheet and Plate, ASTM International, West Conshohocken, PA, USA, 2014.
- [42] K. Wei, M. Gao, Z. Wang, X. Zeng, Effect of energy input on formability, microstructure and mechanical properties of selective laser melted AZ91D magnesium alloy, Mater. Sci. Eng. A 611 (2014) 212–222, <https://doi.org/10.1016/j.msea.2014.05.092>.
- [43] T. Deb Roy, H.L. Wei, J.S. Zuback, T. Mukherjee, J.W. Elmer, J.O. Milewski, A.M. Beese, A. Wilson-Heid, A. De, W. Zhang, Additive manufacturing of metallic components – process, structure and properties, Prog. Mater. Sci. 92 (2018) 112–224, <https://doi.org/10.1016/j.pmatsci.2017.10.001>.
- [44] J.H. Martin, B.D. Yahata, J.M. Hundley, J.A. Mayer, T.A. Schaedler, T.M. Pollock, 3D printing of high-strength aluminium alloys, Nature 549 (2017) 365–369, <https://doi.org/10.1038/nature23894>.
- [45] V. Manakari, G. Parande, M. Gupta, Selective laser melting of magnesium and magnesium alloy powders: a review, Metals 7 (2017) 2, <https://doi.org/10.3390/met7010002>.
- [46] I. Kelbassa, A. Weisheit, K. Wissenbach, V. Hermes, Laser metal deposition of TiAl alloys, 2nd Pacific Int. Conf. Appl. Lasers and Optics (PICALO), 2006 <https://doi.org/10.2351/1.5056929>, paper 705.
- [47] A. Singh, A. Ramakrishnan, D. Baker, A. Biswas, G.P. Dinda, Laser metal deposition of nickel coated Al 7050 alloy, J. Alloys Compd. 719 (2017) 151–158, <https://doi.org/10.1016/j.jallcom.2017.05.171>.
- [48] M. Salehi, S. Maleksaeedi, H. Farnoush, N.M.L. Sharon, G.K. Meenashisundaram, M. Gupta, An investigation into interaction between magnesium powder and Ar gas: implications for selective laser melting of magnesium, Powder Technol. 333 (2018) 252–261, <https://doi.org/10.1016/j.powtec.2018.04.026>.
- [49] I. Zhirnov, D.V. Kotoban, A.V. Gusarov, Evaporation-induced gas-phase flows at selective laser melting, Appl. Phys. A Mater. Sci. Process. 124 (2018), 157. <https://doi.org/10.1007/s00339-017-1532-y>.
- [50] O. Levi, B. Tal, S. Hileli, A. Shapira, I. Benhar, P. Grabov, N. Eliaz, Optimization of EGFR high positive cell isolation procedure by design of experiments methodology, Cytometry B Clin. Cytom. 88 (2015) 338–347, <https://doi.org/10.1002/cyo.b.21246>.
- [51] A.B. Spierings, M. Schneider, R. Eggenthaler, Comparison of density measurement techniques for additive manufactured metallic parts, Rapid Prototyp. J. 17 (2011) 380–386, <https://doi.org/10.1108/13552541111156504>.
- [52] J.A. Slotwinski, E.J. Garboczi, K.M. Hebenstreit, Porosity measurements and analysis for metal additive manufacturing process control, J. Res. Natl. Inst. Stand. Technol. 119 (2014) 494–528, <https://doi.org/10.6028/jres.119.019>.
- [53] W.W. Wits, S. Carmignato, F. Zanini, T.H.J. Vaneker, Porosity testing methods for the quality assessment of selective laser melted parts, CIRP Ann. Manuf. Technol. 65 (2016) 201–204, <https://doi.org/10.1016/j.cirp.2016.04.054>.
- [54] D.F. Susan, J.D. Puskar, J.A. Brooks, C.V. Robino, Quantitative characterization of porosity in stainless steel LENS powders and deposits, Mater. Charact. 57 (2006) 36–43, <https://doi.org/10.1016/j.matchar.2005.12.005>.
- [55] X. Cao, W. Wallace, J.-P. Immarigeon, C. Poon, Research and progress in laser welding of wrought aluminum alloys. II. Metallurgical microstructures, defects, and mechanical properties, Mater. Manuf. Process. 18 (2003) 23–49, <https://doi.org/10.1081/AMP-120017587>.
- [56] M. Pastor, H. Zhao, T. Deb Roy, Continuous wave-Nd: yttrium-aluminum-garnet laser welding of AM60B magnesium alloy, J. Laser Appl. 12 (2000) 91–100, <https://doi.org/10.2351/1.521922>.
- [57] H. Wang, Y. Zou, Microscale interaction between laser and metal powder in powder-bed additive manufacturing: conduction mode versus keyhole mode, Int. J. Heat Mass Transf. 142 (2019), 118473. <https://doi.org/10.1016/j.ijheatmasstransfer.2019.118473>.
- [58] W.E. King, H.D. Barth, V.M. Castillo, G.F. Gallegos, J.W. Gibbs, D.E. Hahn, C. Kamath, A.M. Rubenchik, Observation of keyhole-mode laser melting in laser powder-bed fusion additive manufacturing, J. Mater. Process. Technol. 214 (2014) 2915–2925, <https://doi.org/10.1016/j.jmatprote.2014.06.005>.
- [59] C. Zhong, T. Biermann, A. Gasser, R. Poprawe, Experimental study of effects of main process parameters on porosity, track geometry, deposition rate, and powder efficiency for high deposition rate laser metal deposition, J. Laser Appl. 27 (2015), 042003. <https://doi.org/10.2351/1.4923335>.
- [60] S.I. Baik, A. Duhin, P.J. Phillips, R.F. Klie, E. Gileadi, D.N. Seidman, N. Eliaz, Atomic-scale structural and chemical study of columnar and multilayer Re-Ni electrodeposited thermal barrier coating, Adv. Eng. Mater. 18 (2016) 1133–1144, <https://doi.org/10.1002/adem.201500578>.
- [61] E. Kossov, Y. Khoptiar, C. Cytermann, G. Shemesh, H. Katz, H. Sheinkopf, I. Cohen, N. Eliaz, The use of SIMS in quality control and failure analysis of electrodeposited items inspected for hydrogen effects, Corros. Sci. 50 (2008) 1481–1491, <https://doi.org/10.1016/j.corsci.2008.01.016>.
- [62] W. Liu, J.N. DuPont, In-situ reactive processing of nickel aluminides by laser-engineered net shaping, Metall. Mater. Trans. A 34 (2003) 2633–2641.
- [63] A.S. Johnson, S. Shuai, N. Shamsaei, S.M. Thompson, L. Bian, Fatigue behavior and failure mechanisms of direct laser deposited Inconel 718, Solid Freeform Fabrication 2016: Proc. 26th Annu. Int. Solid Freeform Fabrication Symp. – An Additive Manufacturing Conf 2016, pp. 499–511.
- [64] M.N. Ahsan, R. Bradley, A.J. Pinkerton, Microcomputed tomography analysis of intralayer porosity generation in laser direct metal deposition and its causes, J. Laser Appl. 23 (2011), 022009. <https://doi.org/10.2351/1.3582311>.
- [65] L.L. Parimi, G. Ravi, D. Clark, M.M. Attallah, Microstructural and texture development in direct laser fabricated IN718, Mater. Charact. 89 (2014) 102–111, <https://doi.org/10.1016/j.matchar.2013.12.012>.
- [66] I. Kunce, M. Polanski, K. Karczewski, T. Plocinski, K.J. Kurzydlowski, Microstructural characterisation of high-entropy alloy AlCoCrFeNi fabricated by laser engineered net shaping, J. Alloys Compd. 648 (2015) 751–758, <https://doi.org/10.1016/j.jallcom.2015.05.144>.
- [67] N.C. Verissimo, C. Brito, C.R. Afonso, J.E. Spinelli, N. Cheung, A. Garcia, Microstructure characterization of a directionally solidified Mg-12wt.%Zn alloy: equiaxed dendrites, eutectic mixture and type/morphology of intermetallics, Mater. Chem. Phys. 204 (2018) 105–131, <https://doi.org/10.1016/j.matchemphys.2017.10.032>.
- [68] C. Torres-Sánchez, F.R.A. Al Mushref, M. Norrito, K. Yendall, Y. Liu, P.P. Conway, The effect of pore size and porosity on mechanical properties and biological response of porous titanium scaffolds, Mater. Sci. Eng. C 77 (2017) 219–228, <https://doi.org/10.1016/j.msec.2017.03.249>.
- [69] A.Y. Kumar, J. Wang, Y. Bai, S.T. Huxtable, C.B. Williams, Impacts of process-induced porosity on material properties of copper made by binder jetting additive manufacturing, Mater. Des. 182 (2019), 108001. <https://doi.org/10.1016/j.matdes.2019.108001>.
- [70] W. Xu, X. Lu, B. Zhang, C. Liu, S. Lv, S. Yang, X. Qu, Effects of porosity on mechanical properties and corrosion resistances of PM-fabricated porous Ti-10Mo alloy, Metals 8 (2018) 188, <https://doi.org/10.3390/met8030188>.
- [71] X.H. Wang, J.S. Li, R. Hu, H.C. Kou, L. Zhou, Mechanical properties of porous titanium with different distributions of pore size, Trans. Nonferrous Metals Soc. China 23 (2013) 2317–2322, [https://doi.org/10.1016/S1003-6326\(13\)62735-1](https://doi.org/10.1016/S1003-6326(13)62735-1).
- [72] J.A. Choren, S.M. Heinrich, M.B. Silver-Thorn, Young's modulus and volume porosity relationships for additive manufacturing applications, J. Mater. Sci. 48 (2013) 5103–5112, <https://doi.org/10.1007/s10853-013-7237-5>.
- [73] H. Halim, D.S. Wilkinson, M. Niewczas, The Portevin-Le Chatelier (PLC) effect and shear band formation in an AA5754 alloy, Acta Mater. 55 (2007) 4151–4160, <https://doi.org/10.1016/j.actamat.2007.03.007>.
- [74] A. Yilmaz, The Portevin-Le Chatelier effect: a review of experimental findings, Sci. Technol. Adv. Mater. 12 (2011), 063001. <https://doi.org/10.1088/1468-6996/12/6/063001>.
- [75] A. Heidarzadeh, R.V. Barenji, M. Esmaily, A.R. Ilkhichi, Tensile properties of friction stir welds of AA 7020 aluminum alloy, Trans. Indian Inst. Metals 68 (2015) 757–767, <https://doi.org/10.1007/s12666-014-0508-2>.
- [76] H. Kim, Z. Liu, W. Cong, H.C. Zhang, Tensile fracture behavior and failure mechanism of additively-manufactured AISI 4140 low alloy steel by laser engineered net shaping, Materials 10 (2017), 1283. <https://doi.org/10.3390/ma10111283>.
- [77] A. Pineau, A.A. Benzerqa, T. Pardoen, Failure of metals I: brittle and ductile fracture, Acta Mater. 107 (2016) 424–483, <https://doi.org/10.1016/j.actamat.2015.12.034>.
- [78] M. Tisza, Zs. Lukács, High strength aluminum alloys in car manufacturing, IOP Conf. Ser.: Mater. Sci. Eng. 418 (2018), 012033. <https://doi.org/10.1088/1757-899X/418/1/012033>.
- [79] J.C. Benedyk, Aluminum alloys for lightweight automotive structures, in: P.K. Mallick (Ed.), Materials, Design and Manufacturing for Lightweight Vehicles, Woodhead Publishing Ltd, Cambridge, UK 2010, pp. 79–113.
- [80] Aluminum Alloy: Selection and Applications., The Aluminum Association, Inc., Washington, DC, 1998.
- [81] C.B. Fuller, A.R. Krause, D.C. Dunand, D.N. Seidman, Microstructure and mechanical properties of a 5754 aluminum alloy modified by Sc and Zr additions, Mater. Sci. Eng. A 338 (2002) 8–16, [https://doi.org/10.1016/S0921-5093\(02\)00056-4](https://doi.org/10.1016/S0921-5093(02)00056-4).
- [82] L. Zhou, H. Pan, H. Hyer, S. Park, Y. Bai, B. McWilliams, K. Cho, Y. Sohn, Microstructure and tensile property of a novel AlZnMgScZr alloy additively manufactured by gas atomization and laser powder bed fusion, Scr. Mater. 158 (2019) 24–28, <https://doi.org/10.1016/j.scriptamat.2018.08.025>.